Experimental investigation and numerical simulation of chip formation mechanisms in cutting rock-like materials

Aresh, B., Nawaz Khan, F. & Haider, J.

DOI 10.1016/j.petrol.2021.109869
ISSN 0920-4105

Publisher: Elsevier

Experimental Investigation and Numerical Simulation of Chip Formation Mechanisms in Cutting Rock-like Materials

Balaji Aresh[1,*], Fahd N Khan[2], Julfikar Haider[3]

[1]*Faculty of Engineering, Environment, and Computing, Coventry University, Coventry, UK*

[2]*Faculty of Materials and Chemical Engineering, Department of Materials Science, Ghulam Ishaq Khan Institute of Engineering Sciences and Technology, Topi 23640, Pakistan*

[3]*Advanced Materials and Surface Engineering (AMSE) Research Centre, Manchester Metropolitan University, Chester Street, M1 5GD, UK*

***Corresponding author.**

Dr Balaji Aresh

Faculty of Engineering, Environment, and Computing,

Coventry University,

Coventry, UK

Tel: +44-7702-875841

Email: ad5851@coventry.ac.uk

Abstract

In this study, the effects of tool geometry such as rake angle, and cutting parameters such as depth of cut on the cutting forces were studied and correlated with the built-up edge during the material removal process of a rock-like workpiece. Cutting or scratch tests were performed on low and high strength simulated rock-like materials using a tungsten carbide tipped orthogonal drag tool with three different rake angles (0^o, 10^o and 20^o) in a custom-made machining set-up incorporating a high-speed video camera. Force data were measured by a tri-axial dynamometer and a compatible data acquisition system, and specific cutting energy was calculated to assess the material removal performance. Experiments showed that a cutting tool with a 20° rake angle produced an efficient cut. The high-speed video at the cutting edge were analysed to comprehend the formation and growth of the built-up edge. Novel insight was gained by characterising the shape and was observed that the constantly evolving shape was unique to each rake angle used, this creates an apparent rake angle. By varying the rake angle and cutting parameter, the measured cutting force and thrust force showed that the material strength, cutting tool geometry and depth of cut played important roles in removing materials. Higher cutting efficiency was indicated by lower specific cutting energy at higher depth of cut for all cutting conditions. The formation of the crushed zone in relation to the cutting force revealed that the cutting force increased with the size of the crushed zone having two types of chip formation modes: shearing and fracturing. Numerical simulations were performed using a commercially available tool called ELFEN, a hybrid finite-discrete element software package. The simulations correlated well with experimental investigation. The simulations also showed the formation of crushed zone and crack growth as observed experimentally through the use of high-speed video and also shed light on the state of stress state at the cutting edge.

Keywords

Fracture mechanics, Simulated rock, Crushed zone, Specific cutting energy, Rake angle, High speed video, Numerical modelling.

1. Introduction

Rock drilling is not only associated with the search for natural resources such as oil, gas and geothermal energies but also the activities related to collection of geological materials (e.g., cores and cuttings) for scientific research, space exploration, data logging, search for water and mining and civil engineering (Rostamsowlat et al., 2022). Rock drilling tools have evolved over the years, undergoing changes in their design and in the materials used for their manufacturing. The technical feasibility and economic viability of processing of rocks (drilling, cutting, crushing, etc.) and the choice of a rock machining tools are dependant, inter alia, on the rocks.

Modern day rock drill bits are equipped with steel cylinders containing cemented carbide or Polycrystalline Diamond Compacts (PDC) teeth or milled steel with tungsten carbide coating or button inserts (Rostamsowlat et al., 2018). Improvement in the drilling and cutting of rocks needs a better understanding of the breakage and disintegration of the polycrystalline materials. The chip formation occurs in rocks due to elastic brittle deformation (Nishimatsu, 1972; O.D and L, 1974). Figure 1 shows the process of chip formation. As the tool pushes into the workpiece, the material ahead of the extreme cutting edge is crushed into a fine powder, this is known as the ‘crushed zone’ analogous to the built-up edge in metal cutting. The compaction of the crushed zone leads to the formation of a secondary crushed zone, which initiates the formation of a crack. The crack then propagates downwards, extending below the depth of cut and later rapidly rises up to the free surface resulting in a sudden fracture and the formation of a chip. The tool then moves on to meet a fresh face of the workpiece and the process repeats. The crack patterns are complex to understand given the anisotropy present in the brittle materials like rocks and they vary according to the cutting tools used (A. W, 2004; Cook et al., 1984; Dong, 1993; O.D and L, 1974; Suwannapinij, 1975). The study of the state of stress will provide a better understanding of the crack patterns, crack initiation and its propagation. The crushed zone influences the fracturing of rocks; though the fracture mechanism itself is elastic brittle deformation, the zone remains inelastic (Lindqvist and Hai-Hui, 1983) and since it propagates the energy from the tool to the rock, the importance of this zone cannot be overlooked.

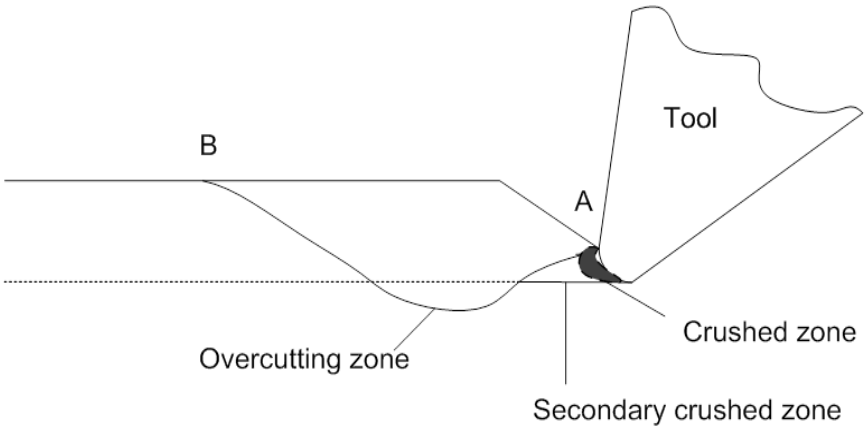

Figure 1. Chip formation model in rock cutting (adapted from [1])

Specific Cutting Energy (SCE) is the energy consumed to remove a unit volume of material. This parameter has been successfully used to characterise the efficiency of a cutting tool in metal cutting (Khan et al., 2014, 2012; Sarwar, 1998; Sarwar et al., 2009, 2007) and it has been used in the drilling industry as a measure of cost per unit volume of rock removed (Atici and Ersoy, 2009) and correlated with other rock properties (Ersoy and Waller, 1995; Mohammadi et al., 2020; Rostamsowlat, 2018; Wang et al., 2018; Yurdakul and Akdasç, 2012).

The equation for calculating the specific cutting energy is given by Equation 1:

$$E_{sp} = \frac{F_c L}{V} \tag{1}$$

where E_{sp} is the specific cutting energy, F_c is the mean cutting force, L is the length of cut, and V is the volume of rock removed.

Atici and Ersoy (2009) studied the specific energy for sawing and drilling of rocks, derived from the energy required to remove a given volume of rock. Low values of SCE indicate efficient cutting. Wang et al. (2018) conducted detailed rock cutting tests, and showed that SCE was not only a function of rock properties but it was closely related to operational parameters such as depth of cut and tool geometry. Huang and Wang (1997) investigated the process of coring of rocks using diamond impregnated drill bits and found a correlation between weight-on-bit (WOB) and SCE. The influence of tool geometry and depth of cut on the drilling of rocks have been found in good correlation in a study conducted by Copur (2010). Ersoy and Waller (1995) studied the relationship between WOB, rate of penetration and SCE and found

that as the WOB increases, so does the penetration rate, with a decrease in SE until an optimum WOB is reached.

The application of SE as performance indicators for roadheaders and tunnel boring machines have been researched by Acaroglu et al. (2008). Cho et al., (2010) used the SCE calculated from numerical simulation to derive the optimum spacing for TBM disc cutters. The influence of depth of cut was studied by Mohammadi et al. (2020) by conducting cutting tests using a chisel shaped cutting tool on various rock types and were able to correlate the debris size to the SCE. SCE was used to develop a new rippability classification system, as it can be easily determined without detailed on-site testing (Basarir et al., 2008).

SCE is often correlated with other rock parameters and efficiency indicators to provide operators with optimum running conditions for all types of rocks. Roxborough (1987) found an increase in SCE as the compressive strength of rocks increase. Coarseness Index (CI) is a comparative size distribution of the rocks. Tuncdemir et al. (2008) successfully correlated CI to SE and formed a statistical relationship defined by Equation 2.

$$SE = \frac{k}{CIn} \tag{2}$$

where k is function of rock strength and cutting tool parameters and n varies from 1.2 to 4.4 based on the cutting tool.

Sengun and Altindag (2013) correlated SCE and the mechanical properties of rocks and found a strong correlation between the density, compressive strength and porosity. Atici and Ersoy (2009) found significant statistical correlation between SCE and the brittleness of rocks. Tiryaki and Dikmen (2006) found positive correlation between SCE and the textural and compositional properties of rocks.

Yadav et al. (2018) conducted cutting experiments on a model soft rock, Gypsum. Through a series of experiments using orthogonal cutting tools, the impact of positive and negative rake angles on the failure mechanism at the cutting edge was assessed. It was identified that for a positive rake angle, the failure mechanism was dominated by fracture and with a negative rake angle, a ductile type failure occurred. High speed camera and image analysis also highlighted a ‘dead zone’ forming at the cutting edge for a negative rake angle cutting tool where compacted particles of gypsum would adhere to the cutting edge. Physical models have long

been employed by engineers to provide qualitative as well as quantitative data (Stimpson, 1970). Qualitative data is provided by the models which maintain geometric similarity, for example, scaled down models of buildings. This study deals with the physical models of the quantitative type where conditions of 'similitude' are maintained. Similitude can be achieved by simulating the physical and mechanical properties of rocks such as their brittle nature, compressive strength and elastic modulus, and as in the case with any other modelling work, it cannot be exact but a fair degree of accuracy can be maintained. The model materials as opposed to the actual rock samples have the advantage of being economically viable to produce or acquire within a short period of time, and being able to change the mechanical properties. Some examples of modelling materials are Portland cement, sand, plaster of Paris and dental plaster to name just a few. Materials are either classified as granular (e.g., sand, chalk, sawdust) or non-granular (e.g., glass, resin, ice), each having distinctive advantages and disadvantages over each other. The ease of sample preparation and time are some of the various factors which influence the choice of the model materials. Tien et al. (2006) used cement and kaolinite to simulate transversely isotropic rock, whereas plaster of Paris was used by Ozbay et al. (1996) to study the fracture process in highly stressed rocks. Sulfaset synthetic rock was used to study the shear stress test by Cho et al. (2008) and a mixture of barite, sand and plaster was used to study crack coalescence by Wong and Chau (1998).

Finite Element Methods (FEM) is a most common numerical method used to solve for a variety of engineering problems, but since it is based on the continuum concept, when applied to rock fracture mechanics, FEM fails to provide useful information when elements are required to open and separate (Jing and Hudson, 2002). Discrete Element Methods (DEM) works on the principle that the system is made up of both rigid and deformable bodies and when deformation/separation occurs then contact between the bodies are continually updated to ensure crack initiation and propagation, this however results in an increase in computational cost (Jing, 2003). DEM has been applied in a variety of problems from soil tilling to rock cutting. Ucgul et al. (2018) applied EDEM a DEM software tool to study the interaction between soil and tillage cutting tool. The cutting performance of conical picks influenced by rock brittleness was studied by Xuefeng et al. (2018) using a DEM software with Particle Flow Code in two dimensions (PFC^{2D}).

Combined Finite element method (FEM) and discrete element method (DEM) is a powerful method to analyse the large number of fractures, since the continuum state of the rock mass

changes to a discontinuum state when the cracks initiate and propagate; this change of state is accomplished by a coupled FEM/DEM method. Carpinteri et al. (2004) used FRANC2D software developed by Cornell University to simulate rock indentation and ploughing on heterogeneous material using a discrete model and homogenous material using a FEM model. They observed stress patterns which indicate tensile parting of cracks and plastic crushing. Cai and Kaiser (2004) successfully used the ELFEN software to simulate the Brazilian Tensile Strength test on homogeneous rock, layered rock and rocks with pre-existing cracks. Li et al. (2021) successfully applied FEM/DEM method to simulate and study crack growth and how it is influenced by rake angle, back rake angle and depth of cut of a PDC cutter. The ELFEN software integrates FEM/DEM to provide a seamless change from continuum state to a discontinuum state.

Although some studies offered a certain degree of understanding on chip formation mechanism, but the scientific knowledge on the interaction between the tool and rock at the extreme cutting edge especially at the microscale level is still lacking. To fill this gap, this research will produce new knowledge of the rock cutting/deformation action at the extreme cutting edge using single cutting tooth test rig, high speed photography to study the built-up edge at the tool tip with synthetic rocks and the use of a coupled discrete/finite element code. The contributions in this work involves preparing artificial rock type materials with specific mechanical properties, develop an experimental set-up with associated instrumentation for cutting force measurement, understanding the chip formation mechanisms at the tool tip with a high speed camera system and conducting extensive experimental work to develop empirical models representing complex relationships among the tool geometry, workpiece materials and depth of cut with the specific cutting energy. Furthermore, numerical simulations were carried out to simulate the material removal process in rock cutting in line with the experimental conditions.

2. Materials and Experimental Methods

2.1. Workpiece specimen preparation

Rock-like workpiece samples were prepared to simulate low strength (LS) and high strength (HS) rocks and tested to record various mechanical properties such as compressive and flexural strength. Granular modelling materials were used in this investigation and Table 1 provides the material composition. The main constituents of the rock-like samples were a mixture of coarse and fine natural aggregates, approximately 5 mm and 1 mm respectively. The binder materials

used were ordinary Portland cement and Silica Fume. Silica Fume in fresh concrete ensures increased cohesion and reduced bleeding. In hardened concretes, the silica fume enhances the mechanical properties (such as compressive strength and modulus of elasticity) and reduces permeability. Polystyrene cubes of 0.001 m^3 by volume were used as the mould for sample preparation.

Table 1. Composition of workpiece materials

Material	**Low strength (LS) workpiece** (kg/m^3)	**High strength (HS) workpiece** (kg/m^3)
Portland cement (BS 12)	240	980
Silica fume	18	100
Coarse aggregate	850	850
Fine sand	275	275
Water (water/cement ratio of 0.35)	84	343

The cement, silica fume, coarse and fine sand were weighed out and added into a concrete mixer rotating at low speed. Water was measured according to the cement content and added steadily into the mixture. The mixing was continued until a desired texture was obtained. The inside surfaces of the polystyrene cubes were coated with a thin film of mould oil to facilitate easy removal of the mould. The mixture was filled into the mould and compacted using a steel tamping rod in layers of 20 mm. Excess concrete was removed, and the top surface was levelled and smoothened carefully. These moulds were left to dry at room temperature for 24 hours. They were then de-moulded and submerged in a curing tank for a further 3 weeks. These samples were used for compressive strength tests and for the linear cutting tests. For the purpose of finding flexural strength and fracture toughness, rectangular moulds measuring 500 × 100 × 100 mm^3 were prepared separately in a similar manner.

2.2 Specimen characterisation

Compressive and flexural strength tests were conducted on the samples in order to accurately define their mechanical properties. Compressive strength tests were conducted according to BS EN 12390-3:2009 using the cube test specimens, while the flexural strength was conducted according to BS EN 12390-5:2009 using the rectangular test specimen on a three-point bend test machine (Denison Mayes Universal Testing Machine) as shown in Figure 2. A constant rate of force was applied to the platens (approximately 3 kN/s) during the compression tests until the

specimen fails. The maximum load was recorded, and the compressive stress was calculated using Equation 3.

$$\sigma_c = \frac{F_c}{A_c} \tag{3}$$

where σ_c is the compressive strength in MPa, F_c is the maximum load at failure, and A_c is the cross-sectional area of the specimen on which the force was applied.

During the flexural tests, the distance between the supporting rollers were maintained at 300 mm and length of the specimen was 500m. A constant loading rate was maintained until the specimen failed, the maximum load was noted, and the flexural strength was calculated using the standard formula.

$$\sigma_f = \frac{F_f L}{2 d_1 d_2^2} \tag{4}$$

where σ_f is the flexural strength in MPa, F_f is the maximum load in N, L is the distance between supporting rollers in mm, and d_1 and d_2 are the width and height of the of the specimen in mm. The average results from the strength tests are shown in Table 2.

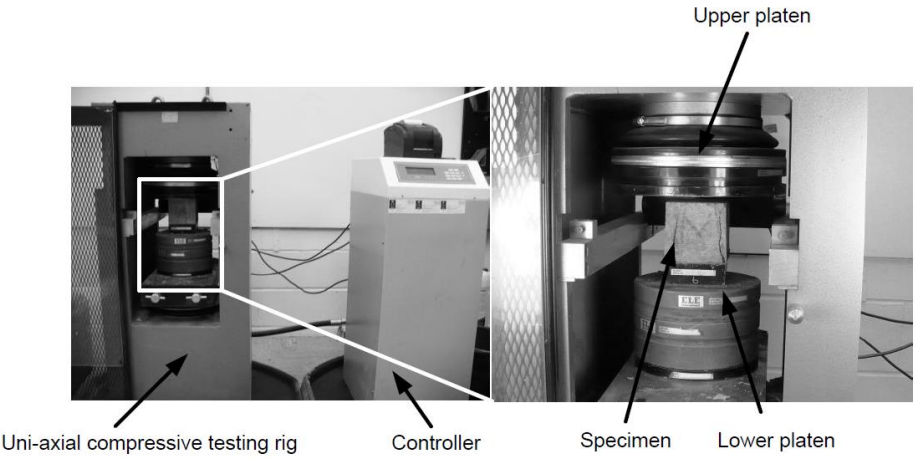

(a)

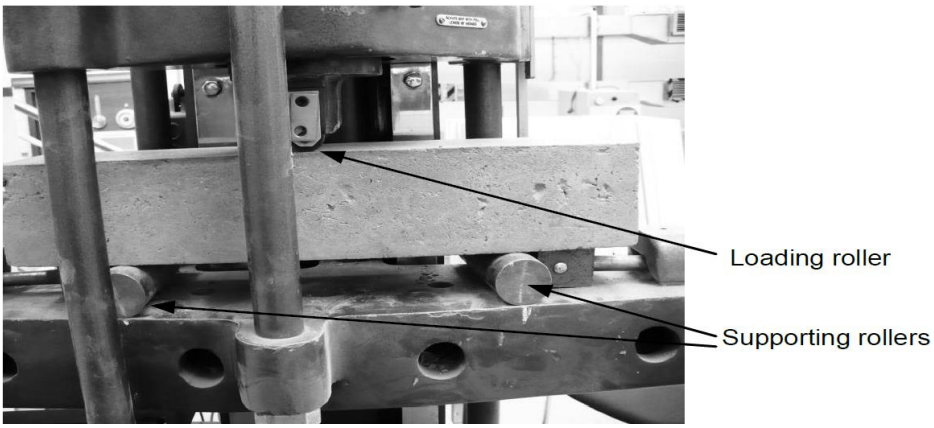

(b)

Figure 2. Experimental set-ups for (a) compressive strength test and (b) flexural strength test

Table 2. Results obtained from the uni-axial mechanical strength test

Sample type	**Flexural strength**		**Compressive strength**		**Density** ρ (kg/m^3)
	σ_f (MPa)	Max. Flexural load F_f (kN)	σ_c (MPa)	Max. compressive load F_c (kN)	
Low strength workpiece (Sample 1)	4.4	8.9	17.5	176	2170
High strength workpiece (Sample 2)	5.7	12.6	53.5	540.4	2190

2.3. Cutting tool

The drag tools used in this investigation were orthogonal cutting tools with brazed tungsten carbide tips. Based on previous literature (Jonak and Gajewski, 2008; Menezes, 2016; Richard et al., 2012; Tiryaki and Dikmen, 2006; Yadav et al., 2018), three cutting tools were designed and used for the cutting tests, each with a 5° clearance angle and rake angles featuring 0°, 10° and 20° as shown in Figure 3. The width, depth and length of the cutting tools used in this investigation were 16 mm, 20 mm and 100 mm respectively.

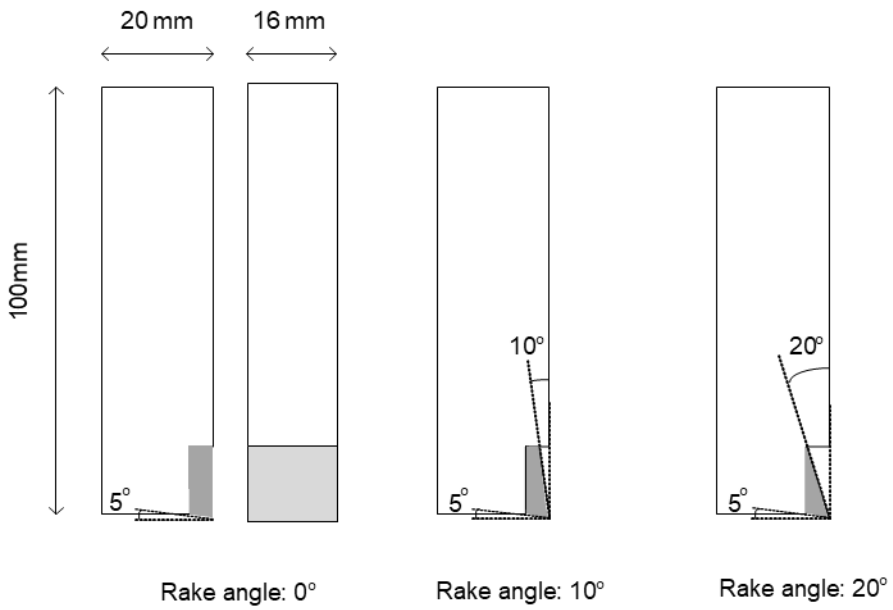

Figure 3. Single point tungsten carbide tipped drag tools used for rock cutting experiments (not to be scaled).

2.4. Linear scratch tests

A test rig was designed and developed by modifying an existing shaper machine to undertake the linear isolated (unrelieved cutting mode) scratch tests on rock-like samples using a single point cutting tool to measure tri-axial cutting forces and to observe the fracture mechanism of the test specimen (Aresh, 2012). The test aimed to gather data on the formation of the crushed zone at the tip of the tool and the initiation of a crack and its propagation and the subsequent ejection of the chip. The schematic diagram of the scratch test rig is presented and elaborated in Figure 4. The test rig was made up of a tool holder, which held an orthogonal drag tool. The cube shaped samples were held in place by the workpiece holder which has an adjustable clamp to ensure a firm grip on the samples. A calibrated tri-axial dynamometer, by Kistler, was fixed on to the table of the shaper machine, this served as a platform for the workpiece holder. The output of the dynamometer was fed into a charge amplifier, the output of which was fed to the computer via a data acquisition device which converted the analogue signals of the dynamometer into digital input. High speed videos of the cutting process made it possible to view and analyse the failure mechanism of the chip and observe the influence of the crushed zone on the cutting process.

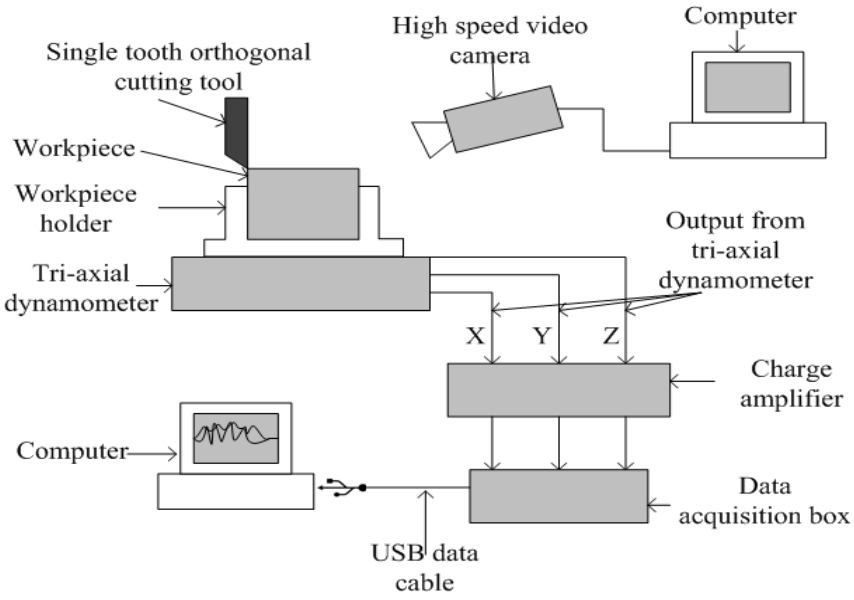

Figure 4. Schematic of the test rig and force components of the tri-axial dynamometer

The tri-axial dynamometer (Kistler 9257B) measured forces along the directions of three axes, the force components are shown in Figure 5, where Fp is the thrust force, Fv is the cutting force and Fs is the side force. As the tool cut through the sample, the three piezo-electric transducers in the dynamometer produce an electrical signal with a magnitude equivalent to the force experienced at the cutting edge. This electrical signal was weak, hence it was fed into a charge amplifier (Kistler 5010A) which amplified the signals and in turn fed them into the data acquisition device. This data acquisition box, by National Instruments (NI USB-6221 BNC) had 8 inputs and interfaced with a computer through a USB cable to convert the analogue input of the charge amplifier to digital output which is read by LabVIEW software on the computer. LabVIEW reads and logs the data; the sampling rate can be defined, and the force measurements are logged into data files. The post-processing of this data was undertaken using Microsoft Excel and MATLAB.

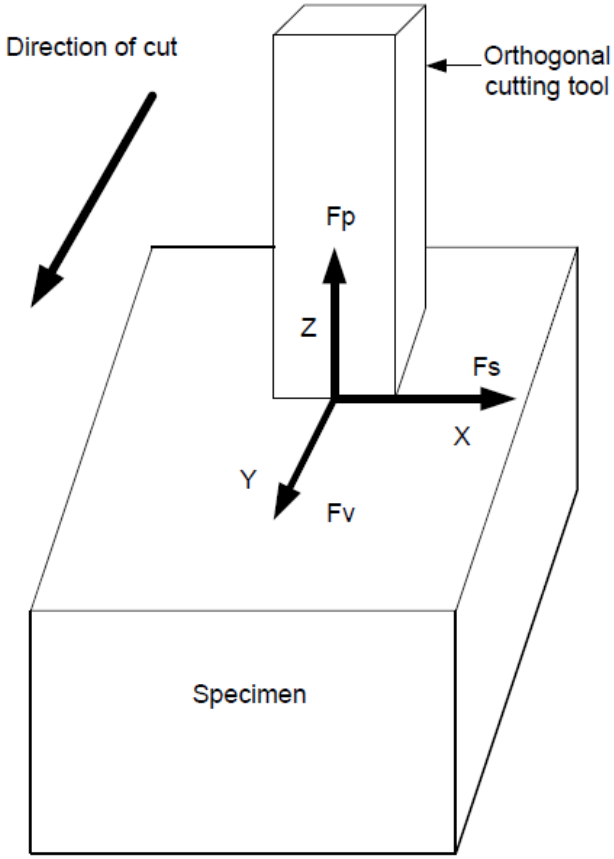

Figure 5. Tri-axial force components measured by the dynamometer during the cutting tests

Scratch tests were performed on the two sets of samples and the parameters that were changed were the depths of cut and rake angles of the drag tool. Preliminary tests were carried out using two cutting speeds (263 mm/s and 333 mm/s) to study the effect on the cutting force. Subsequent scratch tests were performed using 333 mm/s velocity to limit the number of variables in this study. The matrix for experimental tests is presented in Figure 6. The length of cut was 100 mm. The measured cutting forces were used to calculate the SCE for a total of 150 cutting tests using Equation 1. Chips were collected and later visually analysed and categorised according to the sample strength, depth of cut and rake angle.

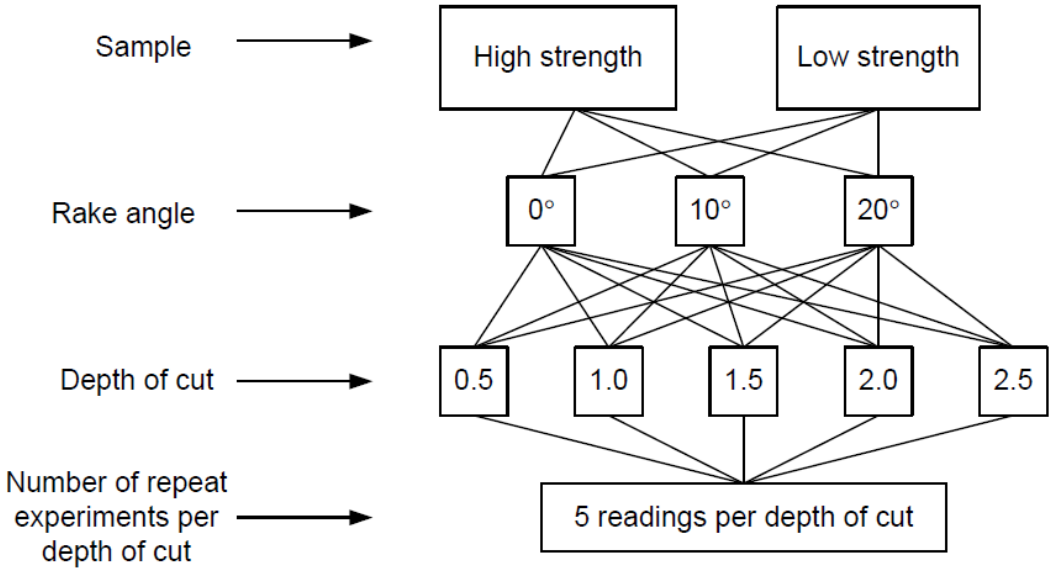

Figure 6. The matrix of cutting experiments on rock-like materials

3. Results and Discussions

A typical force signals recorded by the dynamometer for the cutting and thrust force components at the depths of cut of 0.5 mm and 2.5 mm for the duration of the cut is presented in Figure 7. It was observed that at lower depths of cut, the cutting force (Fv) was lower in magnitude than that of the thrust force (Fp). However, as the depth of cut increased, this feature reversed, indicating that the cutting force turned predominant in magnitude than the thrust force. This was because at lower depth of cut the material failure mechanism was predominately ductile and hence the force required to cut was less and more akin to rubbing the surface. However, as the depth of cut increased, the failure mechanism of the material ahead of the tool tip was identified as fracture and hence the cutting force increased. This was observed for all tests irrespective of the sample type or the rake angle used in this study and also aligned with the results of another study by Mehdi *et al.* (Mohammadi et al., 2020) where cutting tests were conducted on concrete using an orthogonal cutting tool. The nature of these signals was representative of the brittle nature of the workpieces; it could be observed that as soon as the tool impacted with the rock-like workpiece, there was a gradual but a sudden rise in the cutting force (approximately 1000 N and 6000 N for LS and HS workpieces respectively). As the tool ploughs further into the workpiece, cracks initiated usually under the tool tip and propagated down before turning up and reaching the free surface thus producing a chip and the cutting force suddenly dropped. Ejection of the chip from the surface took place

usually at high speed up to 4 m/s as recorded by the use of high-speed video. This high-speed ejection of the chip was represented by a spike in the thrust force. This cycle of local maxima and minima of the cutting and thrust forces repeated for the entire duration of the cut, signifying the brittle breaking off of the chip from the surface of the workpieces.

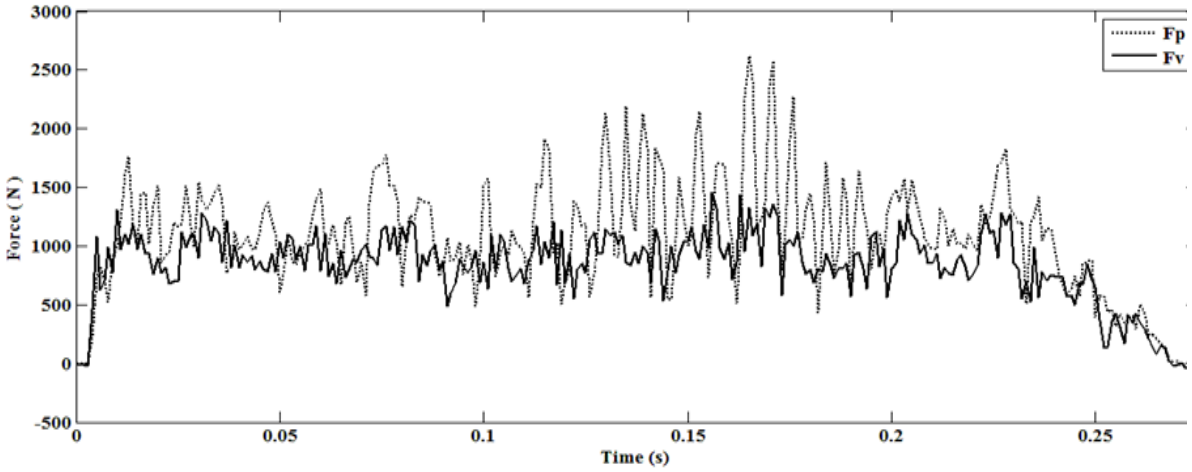

(a)

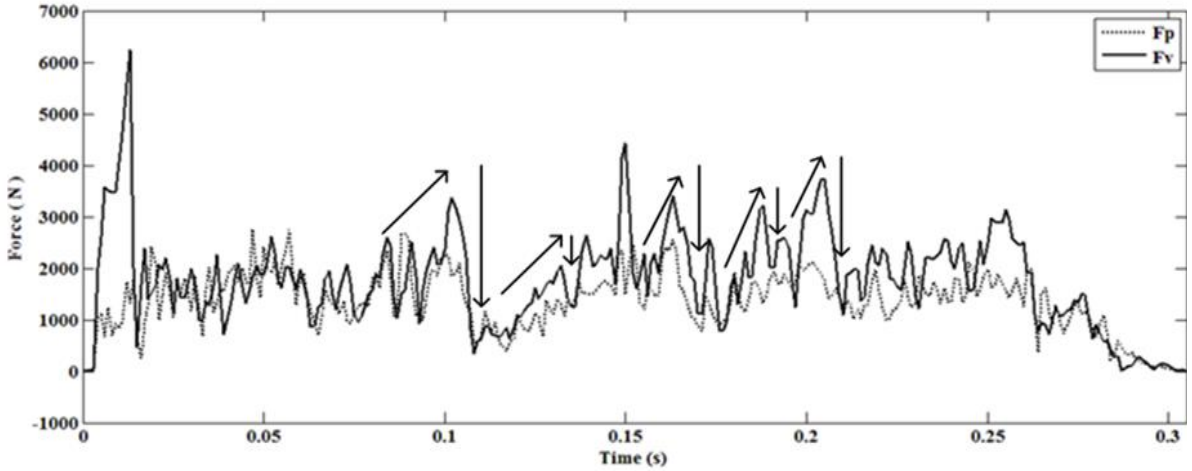

(b)

Figure 7. Variation of the cutting and thrust force with increase in depths of cut (a) 0.5 mm and (b) 2.5 mm

At shallow depths of cut (less than 1 mm) the cutting and thrust force signals were observed to be continuous, as seen in Figure 7(a), while at greater depths, the force signals take the form of a 'saw-tooth' profile, as seen in Figure 7(b) indicated by the arrows. The cutting events could be distinctly recognised, for example, between 0.1s and 0.15s in Figure 7(b) the cutting force was seen to gradually rise even though it was interspersed with local maxima and minima, indicating the formation of minor chips and the crushed zone ahead of the tool tip. The crushed zone was a region of highly compacted powdered material and crucial for the transmission of

the cutting force from the tool to the workpiece and the saw-tooth profile of the cutting force was characteristic of the constant build-up and breaking-off of this crushed zone as observed using high speed video recordings.

3.1. Effect of cutting velocity on the cutting force

Supplementary experiments were conducted to verify the influence of the cutting speeds on the cutting force at the depths of cut, and for the rake angles and workpiece materials used. The shaper machine had two-speed settings of 263 mm/s and 333 mm/s. Figure 8 provides the results of the experiment with the two speed settings. In general, at higher rake angles (10^o and 20^o), the cutting forces decreased with the increase of the cutting speeds for all depths of cut and for both materials. However, at 0^o rake angle, no noticeable changes were seen in the cutting forces with an increase in the cutting speeds. Furthermore, it was observed that data was unavailable for depths greater than 1.5 mm at the slower speed setting of 263 mm/s for the HS workpiece specimen. This was due to the fact that the machine stalled and failed to complete the cut. Therefore, lower cutting speed was not considered for developing a reliable cutting model.

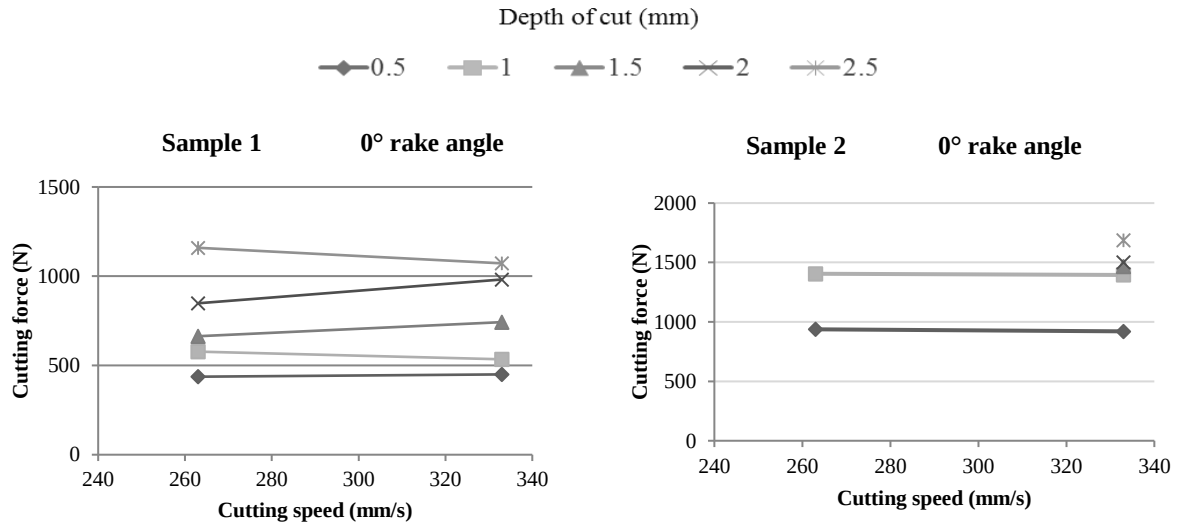

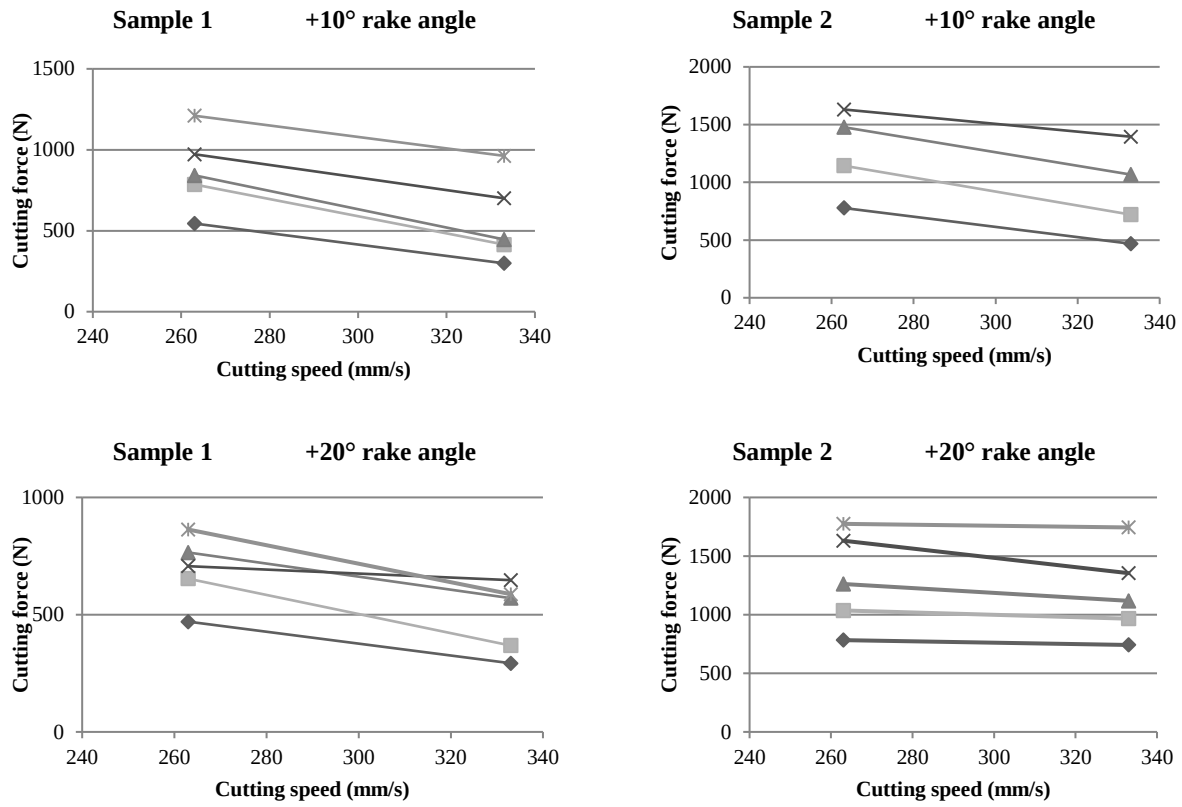

Figure 8. Variation of the cutting force against change in cutting velocity

3.2. Effect of depth of cut and rake angle on the cutting force

Figure 9 shows the Fv and Fp variations against the depths of cut for the two different workpieces and three different rake angles. The cutting force increased with an increase in the depths of cut. However, the thrust force component was seen rather to fluctuate around the mean force of 600 N for the LS workpiece and around 1000 N for the HS workpiece and thus remaining stable for all depths of cut irrespective of the rake angles of the cutting tools. At 0.5 mm depth of cut, it was observed that the rake angles had no significant influence. At these shallow depths of cut the cutting action was analogous to grinding or rubbing action without taking part in material removal action. For all rake angles, the cutting force was observed to be lower than the thrust force. With the increase in the depth of cut, the cutting forces increased at a higher rate than the thrust force and crossed over at a 1.0 mm depth of cut. After this cross-over point, the differences between the cutting and thrust forces increased with an increase in the depths of cut. This was because at lower depths of cut (<1 mm), the failure mechanism of the rock like material was in the ductile regime hence low cutting force was required but as the depth of cut increased, the failure mechanism moved in the brittle regime hence requiring more

force to make the cut as evidenced by the larger debris size (Mohammadi et al., 2020; Richard et al., 2012). For the HS workpiece, the cutting and thrust forces were greatly influenced by the depth of cut particularly at the higher values. Based on the results, it could also be concluded that cutting with a 20° rake angle produced lower magnitudes of Fv and Fp, indicating that an increasing positive rake angle reduced the localised compression of the workpiece at the cutting edge, resulting in lower cutting and thrust forces (Jonak, 2001; Jonak and Gajewski, 2008; Menezes, 2016; Yadav et al., 2018).

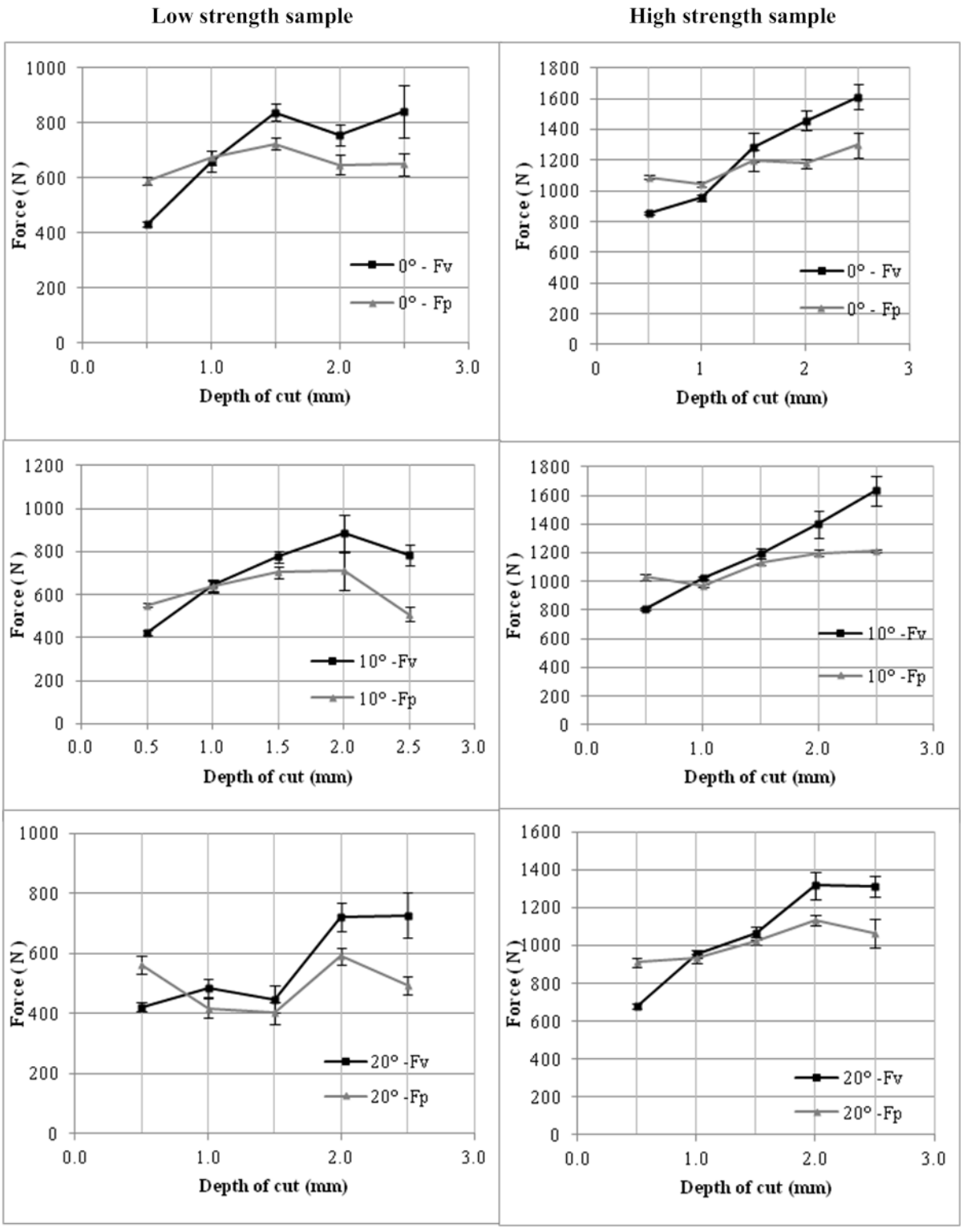

Figure 9. Variation of the cutting force (Fv) and thrust force (Fp) with respect to depths of cut for different rake angles and workpiece materials

3.4. Variation of specific cutting energy

Figure 10 shows effect of the depths of cut on the specific energy for different rake angles and workpieces. General observations showed that SCE decreased with increasing the depth of cut irrespective of the rake angles of the cutting tool or the workpiece materials. This evidence corroborates well with other studies (Cheng et al., 2018; Mohammadi et al., 2020; Zhou et al., 2017). However, the magnitudes of the SCE for HS workpiece were higher than that of the LS workpiece. For example, SCE for the LS workpiece at 0.5 mm depth of cut was approximately 53 MJ/m^3 in contrast to around 101 MJ/m^3 for the HS workpiece. This could be due to the fact that at shallow depth of cut, the failure mechanism was dominated by the ductile failure and the cutting force was influenced by the compressive strength of the material. At larger depths of cut, the failure mechanism was fracture and influenced by the flexural strength of the material (Richard et al., 2012). Furthermore, higher rake angle slightly reduced the SCE at various depths of cut compared to the lower rake angle. Therefore, it can be concluded that the SCE was directly influenced mainly by the depth of cut, compressive strength and flexural strength as corroborated by the other studies (Munoz et al., 2016; Richard et al., 2012).

It should be noted that even though in this study the workpieces are classified as low-strength and high-strength, these samples actually are of very low strength (17.5 MPa) and almost medium strength (53.5 MPa) according to Deere and Miller (1966) classification. However, specific energy values calculated in this study are too high for the above soft rock-like materials. Considering quite low cutting forces generated during the tests, unexpectedly high specific energy values in this study may be attributed to the fracture properties of the artificial rock materials used. Such high specific energy values for such low unconfined compressive strength values may be obtained from evaporitic rocks like polyhalite, potash, trona, and salt. However, evaporitic rocks dominantly exhibit ductile behaviour and fragmentation is not as good as that observed in this study. Therefore, rock-like samples actually did not behave completely like a real rock material in this study.

Cutting at a depth of 0.5 mm requires more energy as work was performed to crush and break the workpiece into fine particles rather than well-formed chips. Figure 11 shows the representative debris collected at various depths of cut using a 10° rake angle cutting tool on the HS workpiece. At this depth of cut, the debris was made up of fine powder and irregular fragments with a maximum diametric size measuring approximately 5 mm. As the depth of cut increased, the fine powder was observed in all the cases but the fragment size increased, reaching nearly 14 mm in diameter at 2.5 mm depth of cut, this has been observed in similar

rock cutting experiments performed by Cheng et al. (2018) granite sandstone and marble. Figure 12 presents the average maximum size of the chips that were formed at various depths of cut and rake angles for LS and HS workpieces. The SCE was observed to decrease as the chip sizes increase, this has been observed in previous research by Mohammadi et al. (2020) on concrete and Friant (1997) where inverse correlation was observed between chip size and SCE. The collected chip sizes from the HS workpiece were slightly larger than those produced from the LS workpiece for all depths of cut and rake angles. This could be attributed to the sample strength as the LS workpiece was easily crushed than the HS workpiece despite both being brittle in nature.

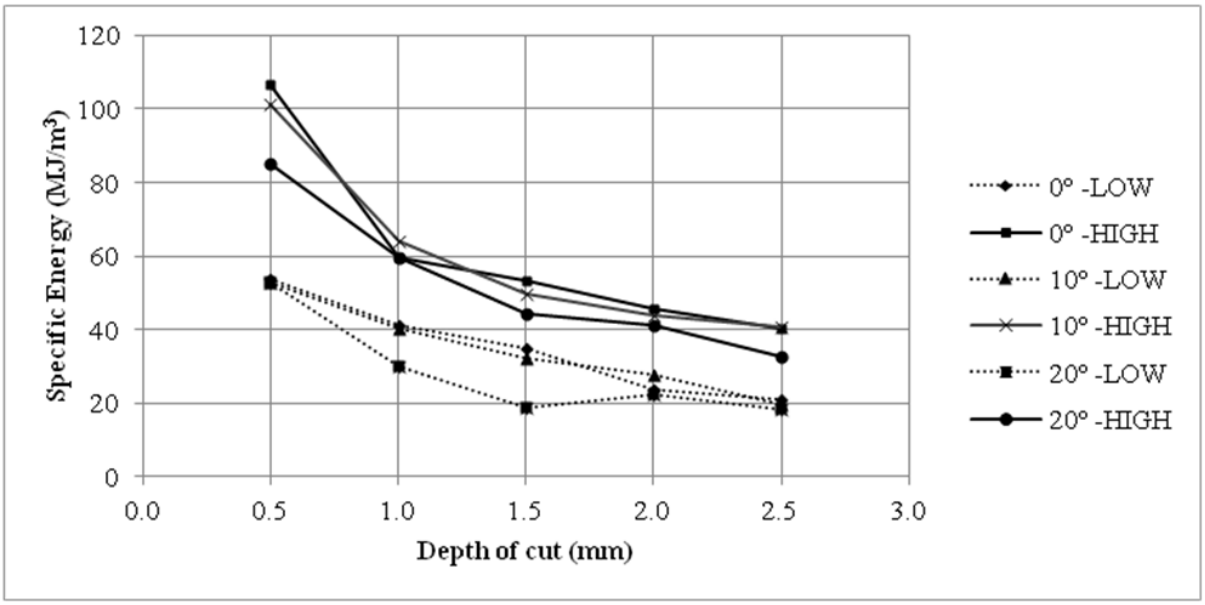

Figure 10. Variation of Specific Cutting Energies with depth of cut, rake angle and sample workpieces.

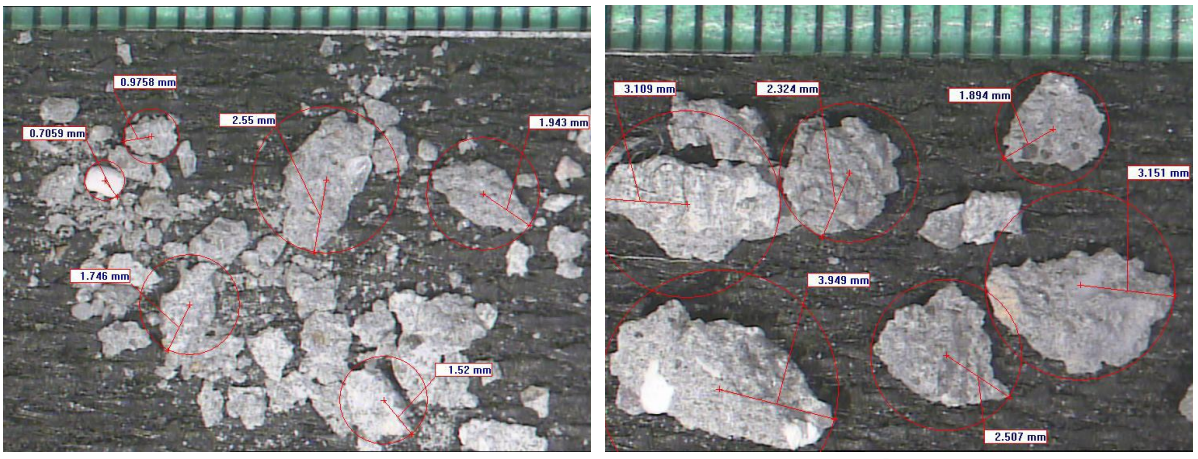

(a) (b)

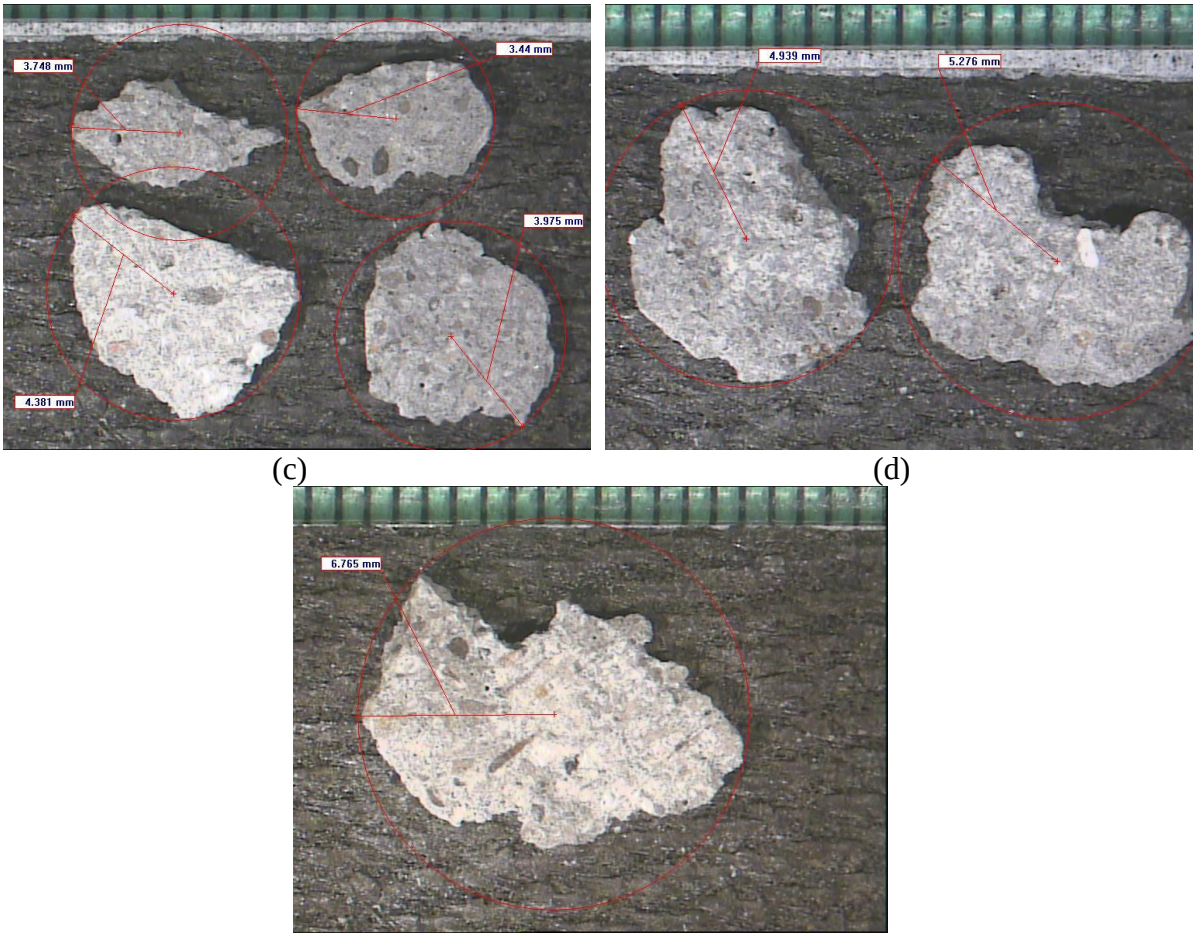

(c) (d)

(e)

395 *Figure 11. Variation of chip size with respect to the depth of cut for 10º rake angle and HS*
396 *workpiece*

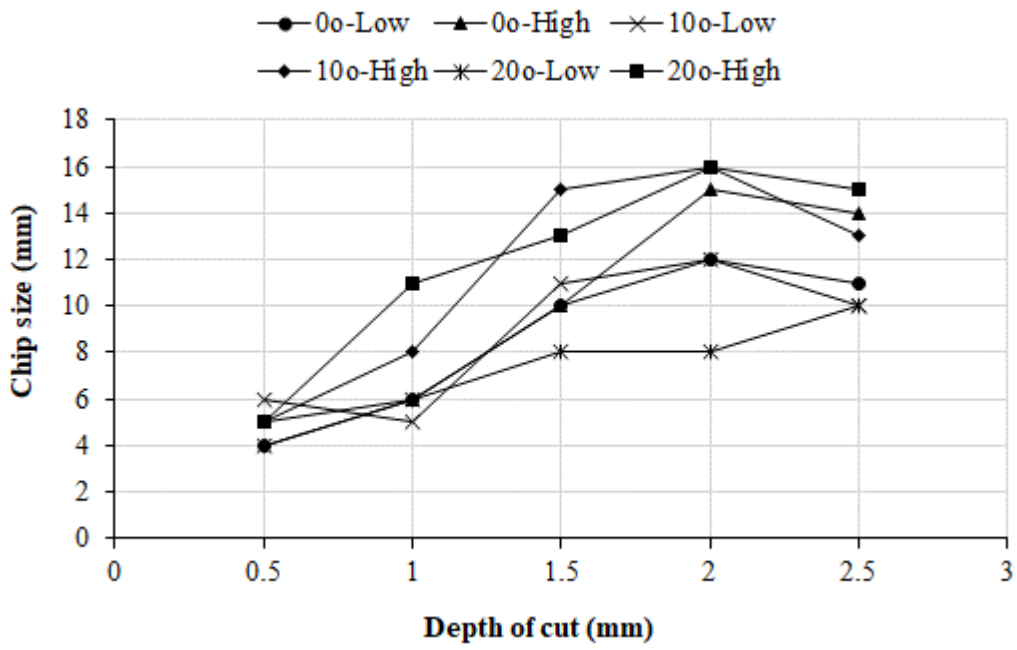

397

Figure 12. Variation of chip size with depth of cut, rake angle and sample workpieces.

3.5. Effect of the Crushed Zone on the Cutting Performance of the Tool

The crushed zone in rock cutting is analogous to the built-up edge in metal cutting, it is crucial to the force transmission from the tool to the rock by building up the stress ahead of the rock to a critical point whereby cracks initiate and propagate.

3.5.1. Characteristics of the crushed zone

High speed video recording of the cutting process was undertaken using a Phantom v7.3 camera produced by Vision Research. The videos were analysed using their proprietary software; features of the crushed zone were extracted and the chip removal process was carefully studied. The shape of the crushed zone was observed to be continuously evolved for the duration of a cut. First, fine crushed material adhered to the tool tip and the deposit built up until a crack forms and produced the chip, and when the chip was ejected from the surface then this crushed zone was also removed completely or partially. In order to study the geometric profile of this zone, the heights and lengths of the crushed zones were measured at the instant of initiation of the chip forming crack from the high-speed video as shown in Figure 13. High speed videos were analysed frame-by-frame and visible major crack system which led to chip formation was chosen. At the point where the crack just began to form, the dimensions of the crushed zone was obtained using the video analysis tool provided by Vision Research.

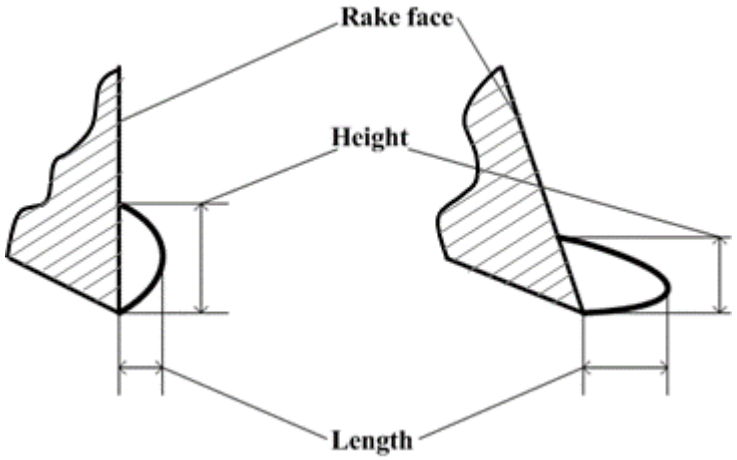

Figure 13. Geometric profile of the crushed zone

Figure 14 and Figure 15 show the height and length distribution of the crushed zones at different depths of cut and rake angles for LS and HS workpieces respectively.

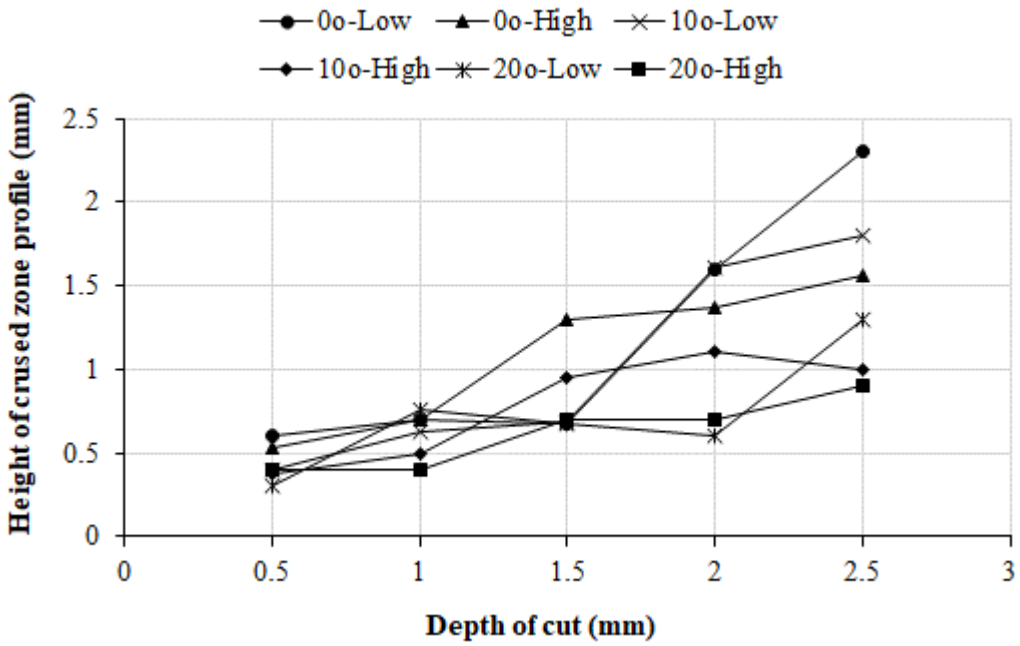

Figure 14. Variation in height of crashed zone with depth of cut, rake angle and sample workpieces.

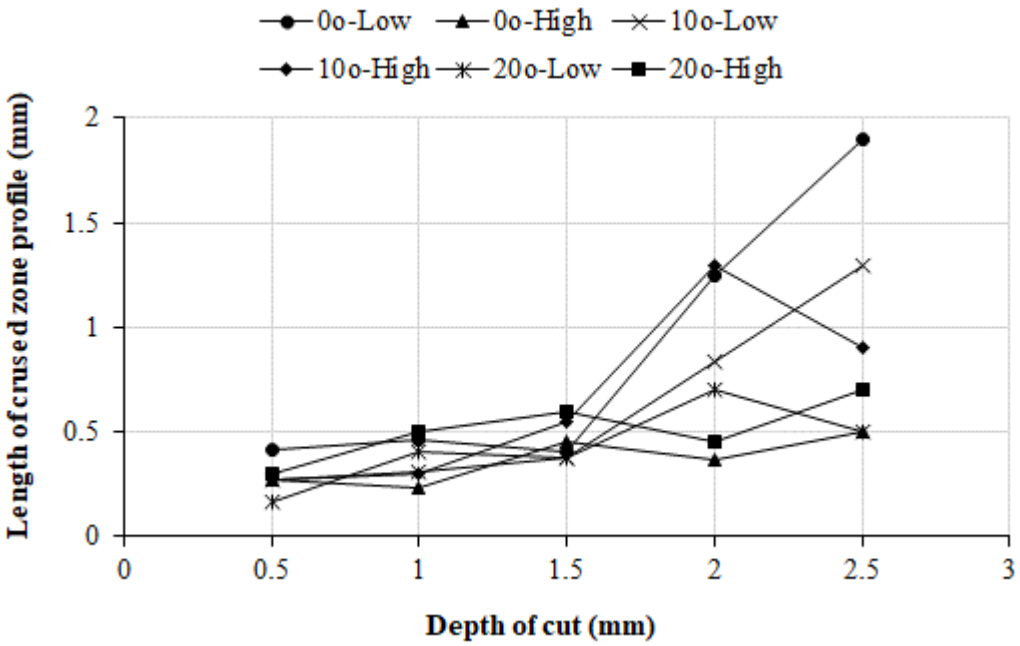

Figure 15. Variation in length of crashed zone with depth of cut, rake angle and sample workpieces.

From the crushed zone measurement, it was found that with an increase in the depth of cut increased the length and width of the crushed zone. The shape of the crushed zone differed based on the rake angle of the cutting tool, as seen in other study (Yadav et al., 2018). In this study, it was observed that the 0° rake angle tool produced crushed zones in the shape of a hemisphere while the 10° and 20° produced wedge-shaped crushed zones as shown in Figure 16. It should be acknowledged that the built-up edge was difficult to see in the still screen captures but they were clearly visible in the high-speed videos.

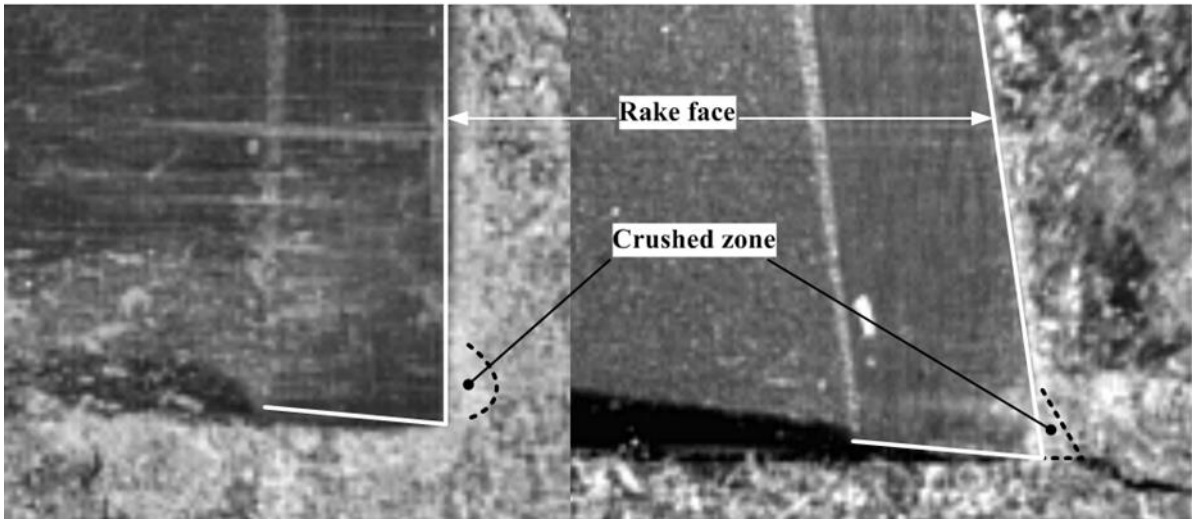

Figure 16. Profile of the crushed zone for different rake angles

Two kinds of chip formation process emerged, as shown in Figure 17, from the high-speed video analysis of the cutting process on both the workpieces and failure always took place due a combination of both:

Mode A: The chip was formed by shearing and this mode occurred in the absence of the crushed zone or when the crushed zone is just building up; and

Mode B: This mode of chip formation was characterised by fracture and was influenced heavily by the crushed zone.

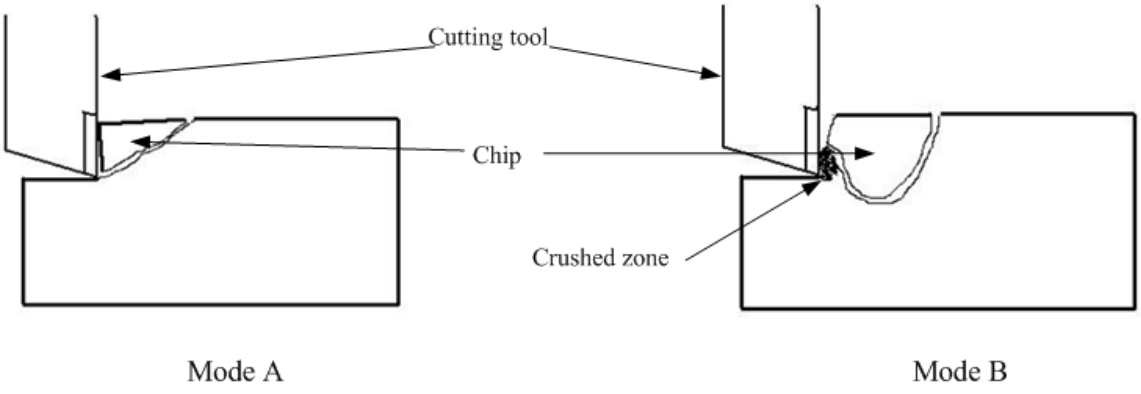

Figure 17. The two types of chip formation mechanism

Deliac and Fairhurst (1988) in their rock cutting experiments involving a pick observed two basic modes of rock failure, one is through a combination of shear/compression fracture and the other is through fracture propagation. In this study, the direction of crack propagation in Mode A failure were observed within a range between 0° - 45° and are not influenced by the rake angle of the tool. When the tool made contact with the workpiece, a crack initiated immediately ahead of the tool tip and propagated to the free surface to produce a chip. Figure 18 shows a sequence of images which shows the Mode A failure in the HS workpiece being cut with a 10° rake angle cutting tool and at 2 mm depth of cut. At 0 second the tool impacted the sample, and at 1.4 ms, cracks were found to have propagated into the sample in a direction parallel to the cut (approximate crack length= 9 mm), as highlighted by arrows. At 1.9 ms the separation took place and a chip was about to be formed and at 2.2 ms the cracks reached the free surface and the chip was ejected from the workpiece surface. It was observed here that the chip already broke into two fragments before ejection. This type of fragmentation of the chip was observed when direction of the crack runs parallel to the free surface.

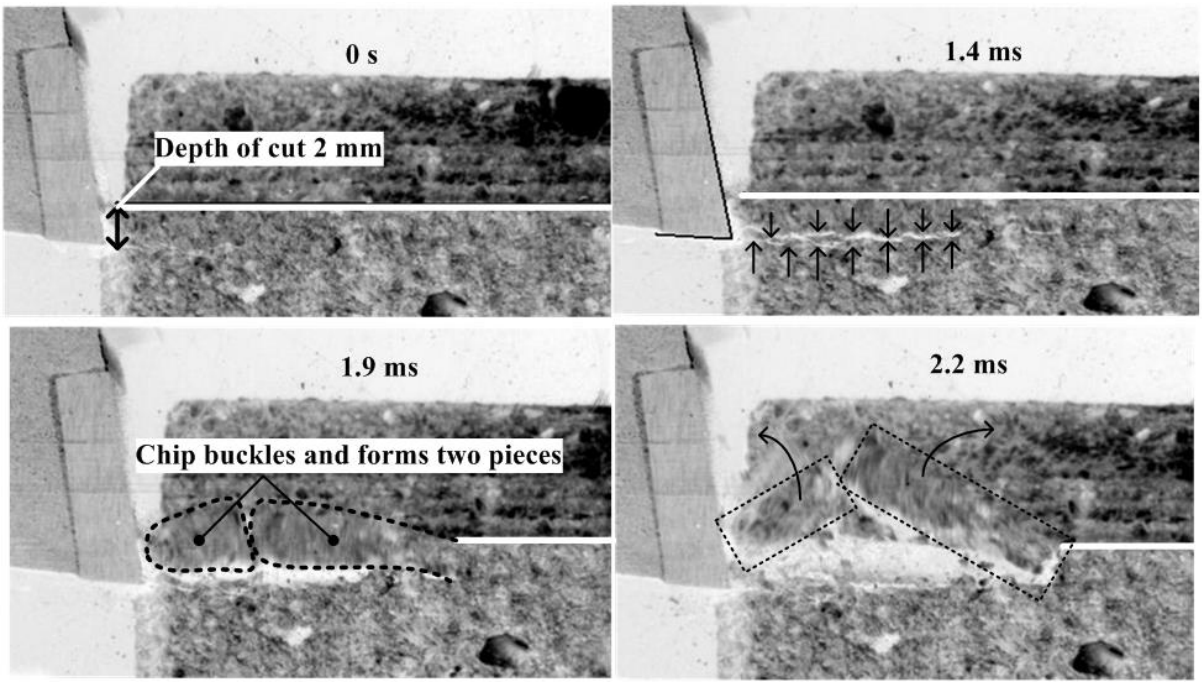

Figure 18. Sequence of images showing the shear failure of a HS workpiece cut with a 10° rake angle at 2 mm depth of cut.

Different types of chip failure were observed from analysing the high-speed video and are represented in a schematic form in Figure 19. Figure 19(a) showed the usually observed chip with the trailing edge thicker than the leading edge. Figure 19(b) was representative of the type of chips formed when the direction of the cracks was parallel to the free surface of the workpiece. The chip behaved as a column and was found to buckle in the middle leading to a splitting up of the original fragment into two. Figure 19(c) shows layered fracture usually observed at depth of cut greater than 2 mm, usually a smaller chip layers off of the surface of the original fragment. The latter two occurrences could be explained by the influence of microcracks radiating away from the tool face; major cracks system coalesce with these microcracks forming the characteristic chip as observed.

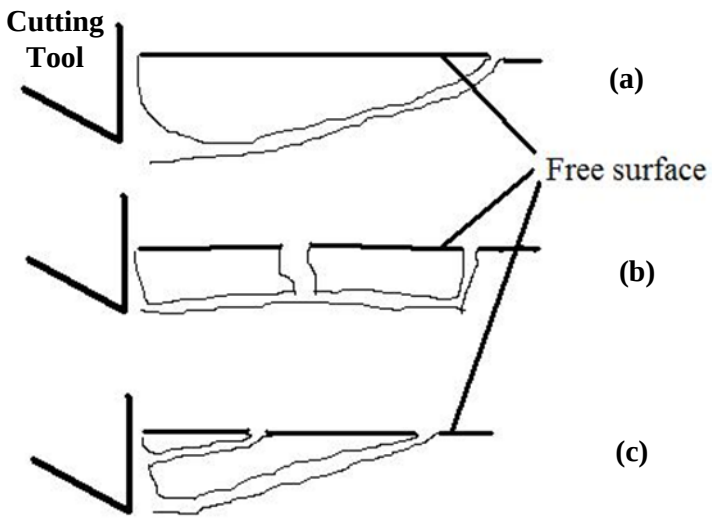

Figure 19. Different types of chip formation observed in type A failure mechanism

In Mode B failure, the chip was formed under the influence of the crushed zone. The crushed zone changed the profile of the tip of cutting tool, thus the original rake angle and the sharp cutting edge became blunt by the crushed zone. The crushed zone as discussed earlier was observed to take primarily two different shapes based on the cutting tool geometry: a hemispherical shape when cutting with a rake angle of 0° and a wedge shape when rake angle is greater than 0°. The shape and size of the crashed zone were critical to the transmission of the force from the tool to the workpiece.

From Figure 16 and Figure 18, it was observed that the crushed zone was formed when fine powdered samples were compacted together to form a dense clump along the tip of the tool. The fine particles flew above or below this dense region and slowly began to adhere to it thus increasing the size of the crushed zone. This crushed material created a region of intense stress and when this reached a critical limit then a crack forms on the upper level of this crushed zone and quickly propagated down into the workpiece and around the crushed zone. It usually propagated below the depth of cut leading to an overcut and then propagated to the free surface and resulted in the formation of the chip.

3.5.2. Force analysis

The crushed zone transmitted the cutting force from the tool to the workpiece. To analyse this event, force trace signals were corroborated with the high-speed video images. Figure 20 shows the cutting and thrust force traces for the HS workpiece being cut with the 0° rake angle tool at

2.5 mm depth of cut. A section of the force trace was highlighted and shown in the figure along with a sequence of images taken during that period. The force trace duration of interest was between 0.1s and 0.13s. It was seen that the cutting force gradually increased from 500 N to 2000 N and so did the thrust force. The signals are interspersed by local maxima and minima peaks during this duration, this is due to microcracks opening up but not leading to a chip formation. This building up of the cutting force and the thrust force coincided with the change in size of the crushed zone as seen in Figure 20. The crushed zone was highlighted by a dashed curve which was seen to evolve in size until a critical point was reached which led to a fracture shown in the last sequence on the right (arrows highlight the path of the crack). Further observation from the video showed that the finely crushed powder 'flow' around the crushed zone all the while compacting it until a critical stress was reached which resulted in fracture propagation. Although Figure 14 and Figure 15 showed some loose trend between the depth of cut and the dimensions of the crushed zone but not significant enough to justify a trend.

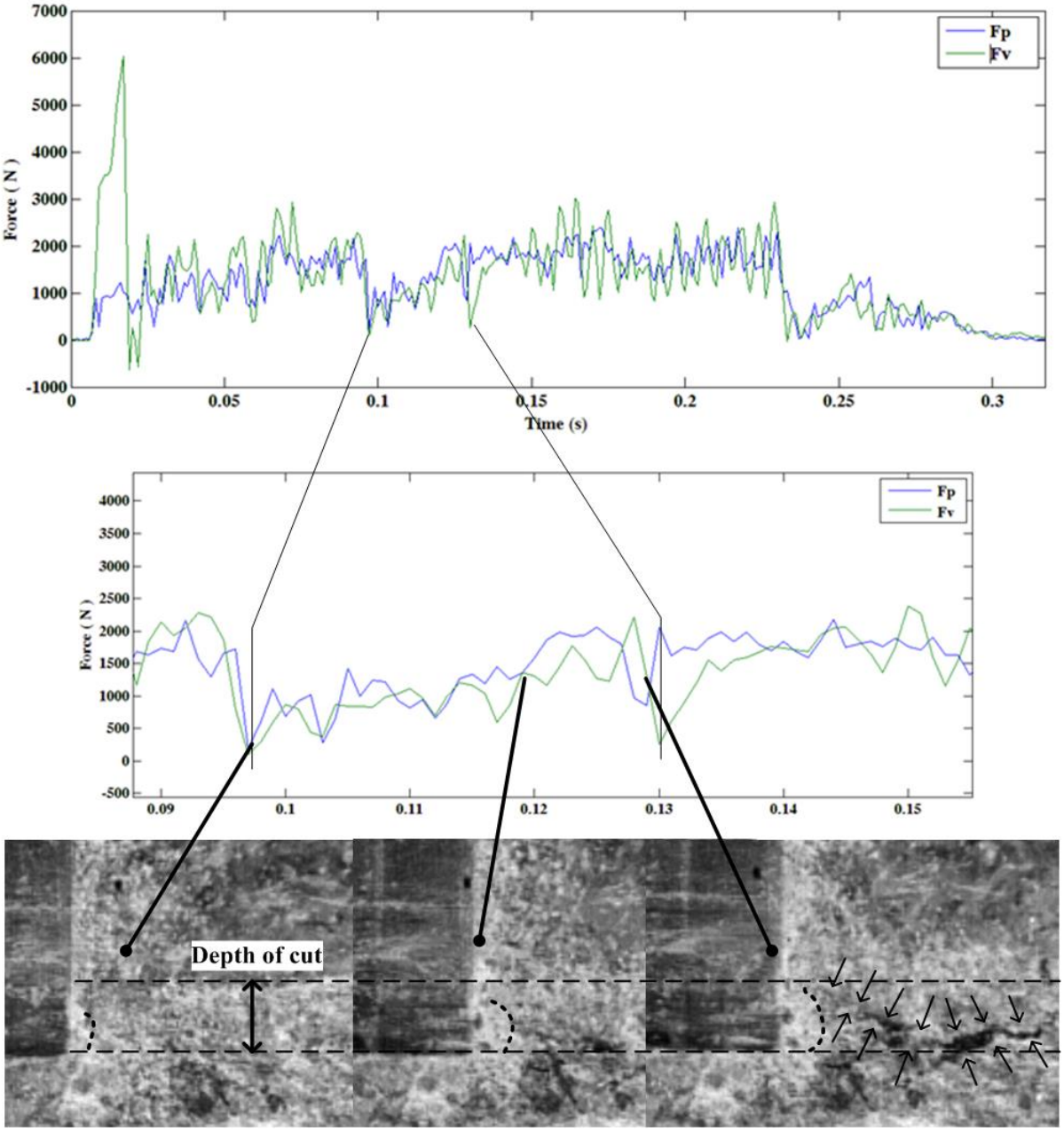

Figure 20. Influence of the crushed zone on the cutting force.

4. Numerical modelling and simulation

A computational model was developed to simulate the rock cutting experiment for further understanding of chip formation mechanism and corroborating the experimental observation. The model used material properties that were found experimentally in this study. Material input parameters were Poisson's ratio, elastic modulus and density. Table 3 lists the material properties for the two types of workpieces and the cutting tool. The material property for the cutting tool was selected so as to make it very stiff (Cai and Kaiser, 2004).

514 *Table 3. Material properties used in numerical simulation*

Material Property	**Value**		
	Cutting tool	HS workpiece (Sample 1)	LS workpiece (Sample 2)
Young's Modulus (GPa)	211	19.4	34.3
Poisson's Ratio	0.286	0.27	0.27
Density (kg/m^3)	7838	2170	2190

515

516 ELFEN explicit solver was used in this research as it was best suited to simulate non-linear
517 fracturing simulations. The 2D geometric model was created in ELFEN by defining points
518 through inputting co-ordinates in the XY plane and then connecting the points by lines. The
519 workpiece dimensions were similar to the experimental workpiece dimension, that is, 100 mm
520 × 100 mm. The points were joined together with lines and the workpiece surface was created
521 by the area enclosed by the lines. The cutting tool was defined in a similar manner with four
522 points, lines and a surface. The cutting tool dimensions were changed according to the rake
523 angles used. The boundary conditions were based on the way the workpiece was secured and
524 the tool held in the tool holder in the experimental test rig. The workpiece had structural fixities
525 applied to the lines on the left and the bottom, and the cutting tool had constraints applied to
526 prevent it from moving in either direction along the y-axis and from rotating about the z-axis.
527 Figure 21 shows the geometric model of the workpiece, cutting tool and the constraints. A
528 mechanical load was applied on the workpiece using a velocity load assigned to the cutting
529 tool, which was equal to the cutting speed of the tool (333 mm/s) in a direction moving from
530 right towards left.

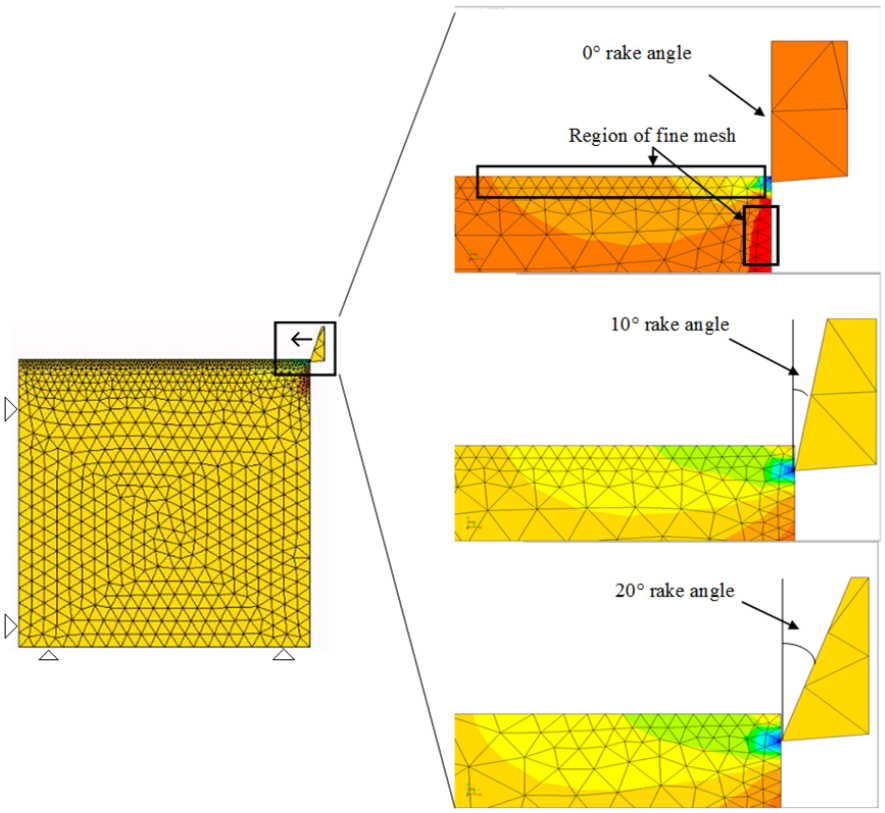

Figure 21. Geometric model of the rock-like sample with constraints and the cutting tool with different rake angles

ELFEN-Explicit offers 13 types of elements covering both 2D and 3D options (Rockfield Software Limited, 2009). In this study, a 2D linear triangular element made up of 3 nodes was used. Each node has 2 degrees of freedom; U and V in the global coordinate system. An unstructured mesh was generated using linear triangular elements with a side length of the element of 5 mm for both the workpiece and the tool, but a finer mesh with side length of 1 mm was generated in the region where the tool interacts with the rock. This was done to produce realistic fracture patterns since the fracture depends on the mesh size and density. The work of Cai and Kaiser (2004) states that crack propagation is dependent on mesh size and density. In a more recent work, van Wyk et al. (2014) also reflects upon the impact of changing mesh size has on the results while Jaime et al. (2015) used the size of the rock particle to define the mesh size. As these numerical simulations form an important tool to study the micromechanics, it was considered important to simulate as close as the experimental observations, hence the debris size collected from the experiments were used as basis of mesh density, at low depth of cut, fine debris approximately 1 mm in diameter were observed, hence the mesh size at the surface was set to 1 mm and at higher depth of cut debris size of

approximately 5mm were observed. The images of the simulation result given are a zoomed in version but when the animation of the results was compared with the high-speed video recordings of the experiments, similarities were observed in crack propagation thus justifying the mesh choice. The cutting tool does not require a fine mesh at the contact regions, and hence, only a few elements with side length of 5 mm were used for mesh generation.

Figure 22 presents a sequence of the simulation of cutting through LS workpiece. At 0.002 ms the tool was seen to contact the workpiece resulting in a region of high compressive stress, which further shrank and concentrated itself to the tool tip as seen at 0.3 ms. At 2 ms, tensile parting occurred and microcracks formed and were observed to propagate down into the sample. The formation of the crushed zone was observed at 5.1 ms which led to major crack initiation as observed at 7.6 ms. At 10 ms, the crack reached the free surface and forms a chip which was ejected; the crushed zone of the workpiece was still seen adhering to the tool tip.

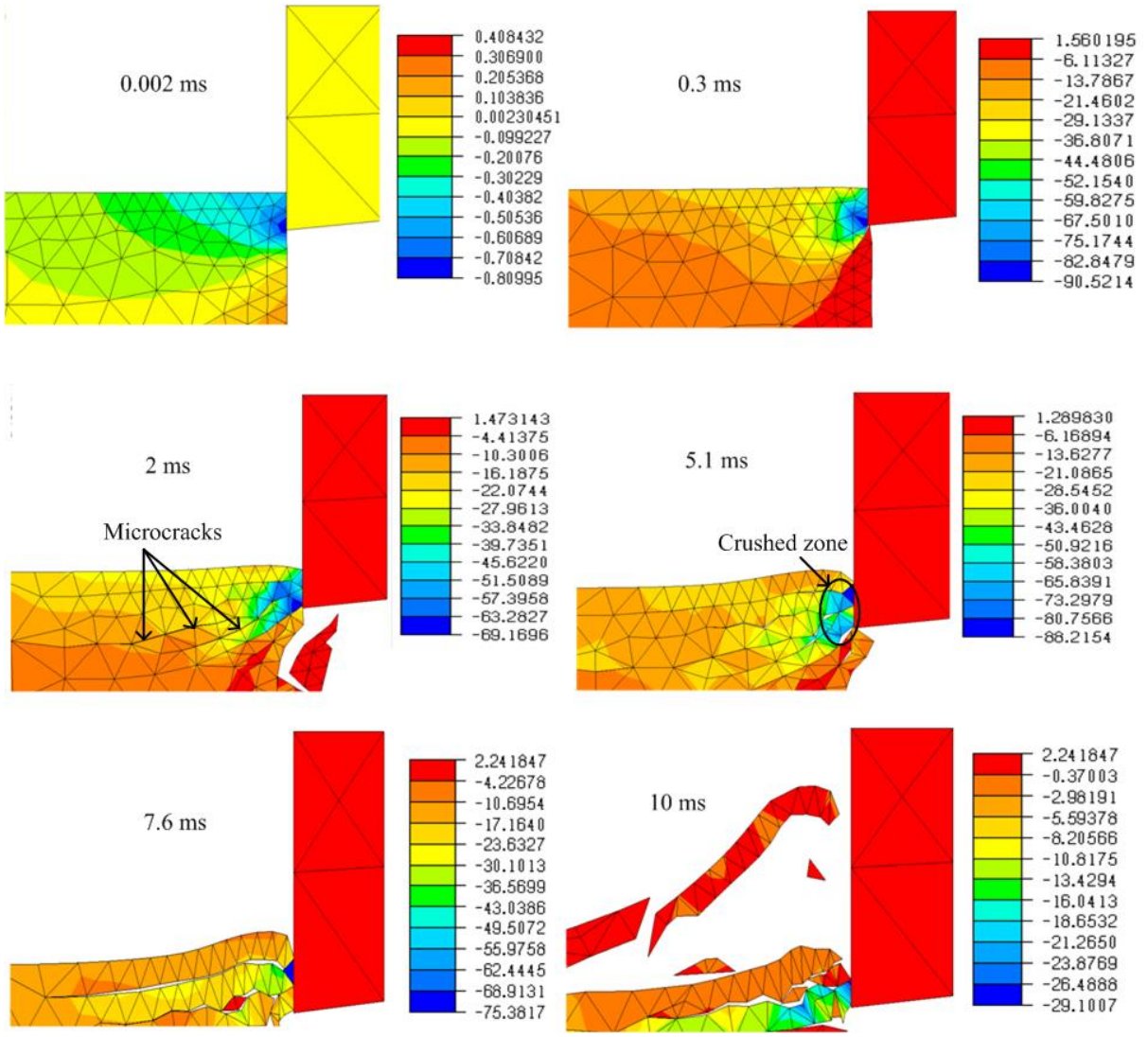

Figure 22. Stress contours of obtained while simulating cutting through a LS workpiece at 0º rake angle and 2 mm depth of cut

Figure 23 shows the stress contours of the cutting simulation of the HS workpiece. It showed cracks propagating from below the tool tip resulting in an over-cut, as seen at a time sequence of 3 ms. At 6.1 ms, a major crack initiated from above the crushed zone and propagated into the workpiece. At 7.1 ms, the cracks reached the free surface resulting in chip formation. The crushed zone was seen intact.

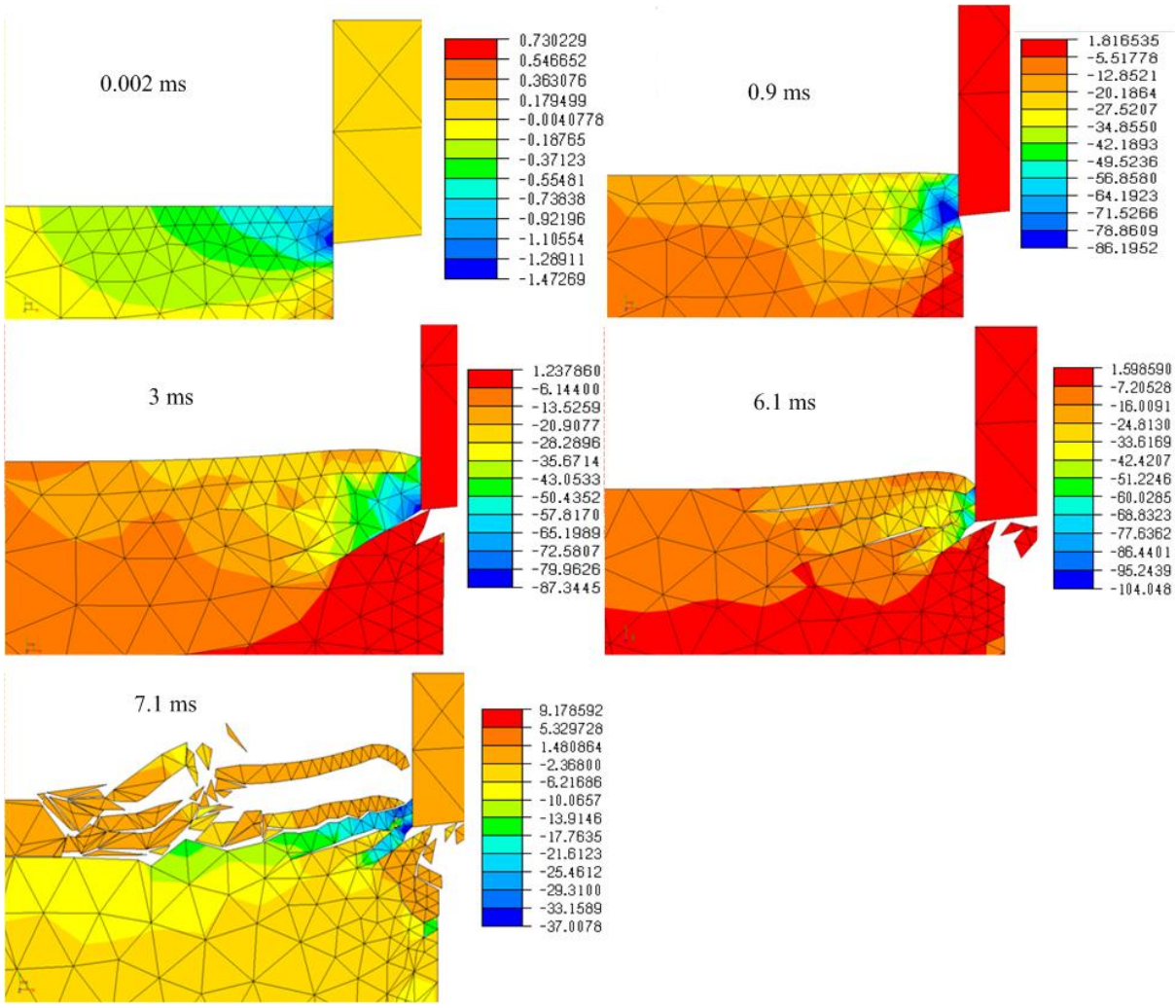

Figure 23. Stress contours obtained while simulating cutting through HS workpiece at 0º rake angle and 2 mm depth of cut

Numerical simulation proved to be an important tool in analysing the stress states ahead of the tool. The results of experimental and numerical simulation produced in this study were found to be similar to a previous work by Zeuch and Finger (1985) who performed cutting test using PDC cutters on three different types of rocks and came to the conclusion that the chip formation process was similar in all rock types and that fractures were nucleated at the cutter tip. They also observed an increase and a drop in the cutting force over the duration of the cut and attributed it to the formation of the crushed zone. Wei et al. (2003) performed cutting tests on Diabase and Granite and concluded that the crushed zone and the chip formation process was formed under the action of tensile stress, which was found to be common observation in all the cuts leading to the build-up of the crushed zone before the crack initiated. The state of stress in the immediate vicinity of the tool tip was critical for the formation of the crushed zone and the crack initiation. Tensile parting of the material leading to the formation of cracks and chips was found as the main mechanism in the simulations carried out in this study. High state of stress was observed during the formation of the crushed zone and microcracks were found to radiate away from this crushed zone. Crack coalescence was clearly observed in all simulations which lead to chip formation. A zone of highly pressurised workpiece at the tool tip was observed for all cuts just as the tool began to cut into the rock, immediately followed by subsurface cracks initiating above and below this zone. It was believed that the crack at the top propagated quicker than the one at the bottom, reaching the free surface and resulting in the formation of the chip. As depth of cut increased, the resulting chip size also increased, this has been observed in the works of Li et al. (2021).

5. Conclusion

In this paper, experimental tests and numerical simulations were carried out to understand the chip removal process in rock-like materials. Linear scratch tests were performed on two different workpiece samples (High Strength, HS and Low Strength, LS) using three different rake angles (0°, 10°, 20°) at shallow depths of cut (0.5, 1, 1.5, 2, 2.5 mm). The following conclusions can be drawn from this research:

1. A novel test set-up was been developed for single point cutting tests with rock like material for controlled experiments; Depth of cut and the sample strength have been identified as the major factors which influence the SCE with minor contribution from the rake angle.

603 2. The mean cutting force in LS workpiece was considerably less, by approximately 50% than
604 those measured in HS workpiece for all rake angles. For both workpieces, it was observed that
605 the 20° rake angle drag tool reduced the cutting force and thrust force needed to make a cut.

606 3. New chip formation mechanism is characterised by brittle failure by a combination of
607 shearing (Mode A) and fracturing (Mode B).

608 4. Crushed zone geometry is influenced by the tool rake angle. The built-up edge consisted of
609 a fine layer of crushed material changes the profile of the tool cutting edge to an apparent rake
610 angle. This profile periodically changed due to either material deposition or detachment from
611 the rake face.

612 5. Numerical simulation results supported the chip formation sequences observed during
613 experiments vis high-speed video to a certain extent.

614 **References**

615

616 Acaroglu, O., Ozdemir, L., Asbury, B., 2008. A fuzzy logic model to predict specific
617 energy requirement for TBM performance prediction. Tunnelling and Underground
618 Space Technology 23, 600–608. https://doi.org/10.1016/J.TUST.2007.11.003

619 Aresh, B., 2012. Fundamental Study into the Mechanics of Material Removal in Rock
620 Cutting. Newcastle upon Tyne.

621 Atici, U., Ersoy, A., 2009. Correlation of specific energy of cutting saws and drilling
622 bits with rock brittleness and destruction energy. Journal of Materials Processing
623 Technology 209, 2602–2612.
624 https://doi.org/10.1016/J.JMATPROTEC.2008.06.004

625 O.D, A., L, D. Mechanism of rock fracture in rotary drilling using a hard alloy bit :
626 alimov, OD frunze polyt. Inst. SU dvornikov, LT frunze polyt. Inst. SU 2F, 16R
627 soviet min. Sci. V8, N6, 1972, P677–682 Int. J. Rock Mech. Min. Sci. Geomech.
628 Abstr. 11, 1974, A41. https://doi.org/10.1016/0148-9062(74)92814-9.

629 Basarir, H., Karpuz, C., Tutluoglu, L., 2008. Specific energy based rippability
630 classification system for coal measure rock. Journal of Terramechanics 45, 51–62.
631 https://doi.org/10.1016/J.JTERRA.2008.07.002

632 Cai, M., Kaiser, P.K., 2004. Numerical Simulation Of The Brazilian Test And The
633 Tensile Strength Of Anisotropic Rocks And Rocks With Pre-Existing Cracks.
634 International Journal of Rock Mechanics and Mining Sciences 41, 478–483.
635 https://doi.org/10.1016/J.IJRMMS.2004.03.086

636 Carpinteri, A., Chiaia, B., Invernizzi, S., 2004. Numerical analysis of indentation
637 fracture in quasi-brittle materials. Engineering Fracture Mechanics 71, 567–577.
638 https://doi.org/10.1016/S0013-7944(03)00037-7

639 Cheng, Z., Sheng, M., Li, G., Huang, Z., Wu, X., Zhu, Z., Yang, J., 2018. Imaging the
640 formation process of cuttings: Characteristics of cuttings and mechanical specific
641 energy in single PDC cutter tests. Journal of Petroleum Science and Engineering
642 171, 854–862. https://doi.org/10.1016/J.PETROL.2018.07.083

643 Cho, J.W., Jeon, S., Yu, S.H., Chang, S.H., 2010. Optimum spacing of TBM disc
644 cutters: A numerical simulation using the three-dimensional dynamic fracturing
645 method. Tunnelling and Underground Space Technology 25, 230–244.
646 https://doi.org/10.1016/J.TUST.2009.11.007

647 Cho, N., Martin, C.D., Sego, D.C., 2008. Development of a shear zone in brittle rock
648 subjected to direct shear. International Journal of Rock Mechanics and Mining
649 Sciences 45, 1335–1346. https://doi.org/10.1016/J.IJRMMS.2008.01.019

650 Copur, H., 2010. Linear stone cutting tests with chisel tools for identification of cutting
651 principles and predicting performance of chain saw machines. International Journal
652 of Rock Mechanics and Mining Sciences 47, 104–120.
653 https://doi.org/10.1016/J.IJRMMS.2009.09.006

654 Deere, D.U., Miller, R.P., 1966. Engineering Classification And Index Properties For
655 Intact Rock. Illinois.

656 Deliac, E.P., Fairhurst, C.E., 1988. Theoretical and practical investigations of improved
657 hard rock cutting systems, in: The 29th U.S. Symposium on Rock Mechanics
658 (USRMS).

659 Ersoy, A., Waller, M.D., 1995. Wear characteristics of PDC pin and hybrid core bits in
660 rock drilling. Wear 188, 150–165. https://doi.org/10.1016/0043-1648(95)06646-2

661 Friant, J.E., 1997. Disc cutter technology applied to drill bits, in: Natural Gas
662 Conference: Emerging Technologies for the Natural Gas Industry.

663 Huang, S.L., Wang, Z.W., 1997. The mechanics of diamond core drilling of rocks.
664 International Journal of Rock Mechanics and Mining Sciences 34, 134.e1-134.e14.
665 https://doi.org/10.1016/S1365-1609(97)00233-5

666 Jaime, M.C., Zhou, Y., Lin, J.S., Gamwo, I.K., 2015. Finite element modeling of rock
667 cutting and its fragmentation process. International Journal of Rock Mechanics and
668 Mining Sciences 80, 137–146. https://doi.org/10.1016/J.IJRMMS.2015.09.004

669 Jing, L., 2003. A review of techniques, advances and outstanding issues in numerical
670 modelling for rock mechanics and rock engineering. International Journal of Rock
671 Mechanics and Mining Sciences 40, 283–353. https://doi.org/10.1016/S1365-
672 1609(03)00013-3

673 Jing, L., Hudson, J.A., 2002. Numerical methods in rock mechanics. International
674 Journal of Rock Mechanics and Mining Sciences 39, 409–427.
675 https://doi.org/10.1016/S1365-1609(02)00065-5

676 Jonak, J., 2001. Influence of Friction in the Problem of Cutting Wedge Penetration into
677 Brittle Materials. Journal of Mining Science 37.
678 https://doi.org/10.1023/A:1015123224716

679 Jonak, J., Gajewski, J., 2008. Identification of ripping tool types with the use of
680 characteristic statistical parameters of time graphs. Tunnelling and Underground
681 Space Technology 23, 18–24. https://doi.org/10.1016/J.TUST.2006.12.002

682 Khan, F., Daadbin, A., Persson, M., Haider, J., 2014. Development of AlTiN coated
683 carbide bandsaw for machining titanium-17 alloy. International Journal of Surface
684 Science and Engineering 8, 11–27.

685 Khan, F.N., Daadbin, A., Persson, M., Haider, J., Hellbergh, H., 2012. Assessing the
686 performance of TiAlSiN coating on bandsaw tooth when cutting Ti-17 alloy.
687 Proceedings of the Institution of Mechanical Engineers, Part B: Journal of
688 Engineering Manufacture 226. https://doi.org/10.1177/0954405411431194

689 Li, Y., Chen, Z., Ye, Y., Yang, Y., 2021. Combined finite-discrete element method for
690 modeling the interaction between single PDC cutter and brittle rock. Journal of
691 Petroleum Science and Engineering 207, 109133.
692 https://doi.org/10.1016/J.PETROL.2021.109133

693 Lindqvist, P.-A., Hai-Hui, L., 1983. Behaviour of the crushed zone in rock indentation.
694 Rock Mechanics and Rock Engineering 16. https://doi.org/10.1007/BF01033280

695 Menezes, P.L., 2016. Influence of friction and rake angle on the formation of built-up
696 edge during the rock cutting process. International Journal of Rock Mechanics and
697 Mining Sciences 88. https://doi.org/10.1016/j.ijrmms.2016.07.013

698 Mohammadi, M., Khademi Hamidi, J., Rostami, J., Goshtasbi, K., 2020. A Closer Look
699 into Chip Shape/Size and Efficiency of Rock Cutting with a Simple Chisel Pick: A
700 Laboratory Scale Investigation. Rock Mechanics and Rock Engineering 53.
701 https://doi.org/10.1007/s00603-019-01984-5

702 Munoz, H., Taheri, A., Chanda, E., 2016. Rock cutting characteristics on soft-to-hard
703 rocks under different cutter inclinations. International Journal of Rock Mechanics
704 and Mining Sciences 87. https://doi.org/10.1016/j.ijrmms.2016.05.014

705 Nishimatsu, Y., 1972. The mechanics of rock cutting. International Journal of Rock
706 Mechanics and Mining Sciences & Geomechanics Abstracts 9, 261–270.
707 https://doi.org/10.1016/0148-9062(72)90027-7

Ozbay, M.U., Dede, T., Napier J.A.L., 1996. Physical and numerical modelling of rock fracture. The Joumal of The South African Institute of Mining and Metallurgy 317–327.

Richard, T., Dagrain, F., Poyol, E., Detournay, E., 2012. Rock strength determination from scratch tests. Engineering Geology 147–148, 91–100. https://doi.org/10.1016/J.ENGGEO.2012.07.011

Rockfield Software Limited, 2009. ELFEN Explicit Manual, Version 4.4. ed. Rockfield Software Limited, Swansea.

Rostamsowlat, I., 2018. Effect of Cutting Tool Properties and Depth of Cut in Rock Cutting: An Experimental Study. Rock Mechanics and Rock Engineering 51. https://doi.org/10.1007/s00603-018-1440-2

Rostamsowlat, I., Akbari, B., Evans, B., 2018. Analysis of rock cutting process with a blunt PDC cutter under different wear flat inclination angles. Journal of Petroleum Science and Engineering 171, 771–783. https://doi.org/10.1016/J.PETROL.2018.06.003

Rostamsowlat, I., Evans, B., Kwon, H.J., 2022. A review of the frictional contact in rock cutting with a PDC bit. Journal of Petroleum Science and Engineering 208, 109665. https://doi.org/10.1016/J.PETROL.2021.109665

Roxborough, F.F., 1987. The role of some basic rock properties in assessing cuttability, in: Proceedings of the Seminar on Tunnels: Wholly Engineered Structures. The Institute of Engineers Australia and AFCC, Sydney.

Sarwar, M., 1998. Application of advanced surface engineering treatments to multi-point cutting edges. Surface and Coatings Technology 108–109, 612–619. https://doi.org/10.1016/S0257-8972(98)00594-5

Sarwar, M., Persson, M., Hellbergh, H., 2007. Wear of the cutting edge in the bandsawing operation when cutting austenitic 17-7 stainless steel. Wear 263, 1438–1441. https://doi.org/10.1016/J.WEAR.2006.12.066

Sarwar, M., Persson, M., Hellbergh, H., Haider, J., 2009. Measurement of specific cutting energy for evaluating the efficiency of bandsawing different workpiece materials. International Journal of Machine Tools and Manufacture 49, 958–965. https://doi.org/10.1016/J.IJMACHTOOLS.2009.06.008

Sengun, N., Altindag, R., 2013. Prediction of specific energy of carbonate rock in industrial stones cutting process. Arabian Journal of Geosciences 6. https://doi.org/10.1007/s12517-011-0429-x

Stimpson, B., 1970. Modelling materials for engineering rock mechanics. International Journal of Rock Mechanics and Mining Sciences & Geomechanics Abstracts 7, 77–121. https://doi.org/10.1016/0148-9062(70)90029-X

Suwannapinij, Sompop, 1975. The mechanical and cutting properties of rocks related to the application of tunnel boring machines. Thesis. https://core.ac.uk/display/153776290. (Accessed 6 November 2021).

Tien, Y.M., Kuo, M.C., Juang, C.H., 2006. An experimental investigation of the failure mechanism of simulated transversely isotropic rocks. International Journal of Rock Mechanics and Mining Sciences 43, 1163–1181. https://doi.org/10.1016/J.IJRMMS.2006.03.011

Tiryaki, B., Dikmen, A.C., 2006. Effects of Rock Properties on Specific Cutting Energy in Linear Cutting of Sandstones by Picks. Rock Mechanics and Rock Engineering 39. https://doi.org/10.1007/s00603-005-0062-7

Tuncdemir, H., Bilgin, N., Copur, H., Balci, C., 2008. Control of rock cutting efficiency by muck size. International Journal of Rock Mechanics and Mining Sciences 45. https://doi.org/10.1016/j.ijrmms.2007.04.010

Ucgul, M., Saunders, C., Fielke, J.M., 2018. Comparison of the discrete element and finite element methods to model the interaction of soil and tool cutting edge. Biosystems Engineering 169, 199–208. https://doi.org/10.1016/J.BIOSYSTEMSENG.2018.03.003

Wang, X., Wang, Q.-F., Liang, Y.-P., Su, O., Yang, L., 2018. Dominant Cutting Parameters Affecting the Specific Energy of Selected Sandstones when Using Conical Picks and the Development of Empirical Prediction Models. Rock Mechanics and Rock Engineering 51. https://doi.org/10.1007/s00603-018-1522-1

Wei, X., Wang, C.Y., Yuan, H.L., Xie, Z.H., 2003. Study of Fracture Mechanism of Rock Cutting. Key Engineering Materials 250. https://doi.org/10.4028/www.scientific.net/KEM.250.200

Wong, R.H.C., Chau, K.T., 1998. Crack coalescence in a rock-like material containing two cracks. International Journal of Rock Mechanics and Mining Sciences 35, 147–164. https://doi.org/10.1016/S0148-9062(97)00303-3

van Wyk, G., Els, D.N.J., Akdogan, G., Bradshaw, S.M., Sacks, N., 2014. Discrete element simulation of tribological interactions in rock cutting. International Journal of Rock Mechanics and Mining Sciences 65, 8–19. https://doi.org/10.1016/J.IJRMMS.2013.10.003

Xuefeng, L., Shibo, W., Shirong, G., Malekian, R., Zhixiong, L., 2018. Investigation on the influence mechanism of rock brittleness on rock fragmentation and cutting performance by discrete element method. Measurement 113, 120–130. https://doi.org/10.1016/J.MEASUREMENT.2017.07.043

780 Yadav, S., Saldana, C., Murthy, T.G., 2018. Experimental investigations on deformation
781 of soft rock during cutting. International Journal of Rock Mechanics and Mining
782 Sciences 105, 123–132. https://doi.org/10.1016/J.IJRMMS.2018.03.003

783 Yurdakul, M., Akdasç, H., 2012. Prediction of specific cutting energy for large diameter
784 circular saws during natural stone cutting. International Journal of Rock Mechanics
785 and Mining Sciences 53, 38–44. https://doi.org/10.1016/J.IJRMMS.2012.03.008

786 Zeuch, D.H., Finger, J.T., 1985. Rock breakage mechanisms with a PDC cutter, in:
787 Conference: Annual Technical Conference and Exposition of the Society of
788 Petroleum Engineers. Las Vegas.

789 Zhou, Y., Zhang, W., Gamwo, I., Lin, J.-S., 2017. Mechanical specific energy versus
790 depth of cut in rock cutting and drilling. International Journal of Rock Mechanics
791 and Mining Sciences 100. https://doi.org/10.1016/j.ijrmms.2017.11.004

792

793